International Journal of Solids and Structures 45 (2008) 4384–4406

Contents lists available at ScienceDirect

International Journal of Solids and Structures

journal homepage: www.elsevier.com/locate/ijsolstr

On the dissipative zone in anisotropic damage models for concrete

P. Pröchtel *, U. Häußler-Combe

Institute of Concrete Structures, Technische Universität Dresden, 01062 Dresden, Germany

ARTICLE INFO

Article history:
Received 16 July 2007
Received in revised form 19 March 2008
Available online 27 March 2008

Keywords:
Damage mechanics
Anisotropy
Thermodynamics
Principle of maximum dissipation rate
Crack band approach
Fracture energy approach
Localization
Dissipative zone
Regularization

ABSTRACT

This paper presents a three-dimensional model to simulate the behavior of plain concrete structures that are predominantly tensile loaded. This model, based on continuum damage mechanics, uses a symmetric second-order tensor as the damage variable, which permits the simulation of orthotropic degradation. The validity of the first and the second law of thermodynamics, as well as the validity of the principle of maximum dissipation rate, are required. That is attained by defining the loading functions in quantities that are thermodynamically conjugated to the damage variables. Furthermore, the evolution rule is derived by maximizing the energy dissipation rate. This formulation is regularized by means of the fracture energy approach by introducing a characteristic length. The basic and new idea in this paper is that the characteristic length should always coincide with the width of the dissipative zone appearing in the simulation. The integration points with increasing damage in one loading increment are the dissipative zone in this loading increment. The main objective of this paper is the convenient formulation of approaches for the characteristic length in order to attain the coincidence of the characteristic length with the width of the dissipative zone appearing in the simulation. It is shown that simulations are objective and yield good results if the requirement is fulfilled that the characteristic length in the constitutive law coincides with the width of the dissipative zone in the simulation.

1. Introduction

The tensile behavior of normal concrete, beyond its linear elastic range, is defined by the formation and growth of microcracks. Over time, concentration and coalescence of these micro-defects in a process zone lead to the appearance of macrocracks. By observing the uniaxial, macroscopic behavior, one clearly sees the softening of concrete and a loss of stiffness in concrete as proven by cyclic tensile tests, (Gopalaratnam and Shah, 1985). Modeling of these properties can be formulated by means of continuum damage mechanics, (Lemaitre, 1991; Carol et al., 1994; Krajcinovic, 1996), by applying such concepts as isotropic or anisotropic damage. The anisotropic damage concept should be used for simulating the tensile softening behavior of normal concrete due to the orientation of the resulting load-induced microcracks. Many different anisotropic damage models exist and one possible way to characterize the different formulations is to distinguish them based on the chosen damage variables: (Krajcinovic and Fonseka, 1981) represented the damage with vectors; (Govindjee et al., 1995; Murakami and Kamiya, 1996; Dragon et al., 2000 and Carol et al., 2001a) used a second order tensor; (Papa and Taliercio, 1996 and Berthaud et al., 1990) applied a combination of second order tensors and scalars; (Chaboche, 1993) suggested a fourth order tensor and models that use directly the stiffness or the compliance to represent the damage were suggested by Simo and Ju (1987a,b) and Pölling (2000). Anisotropic damage models are primarily defined by either a strain-based or a stress-based loading surface. As shown in Section 2.2, a promising approach is the formulation of loading functions in the space of the variables that are ther-

* Corresponding author. Tel.: +49 351 463 36912; fax: +49 351 463 37279.
E-mail address: Patrick.Proechtel@tu-dresden.de (P. Pröchtel).

0020-7683/$ - see front matter © 2008 Elsevier Ltd. All rights reserved.
doi:10.1016/j.ijsolstr.2008.03.015

modynamically conjugated to the damage variables designated as dissipative forces. A physically reasonable way to derive an evolution law for the damage variables is to maximize the energy dissipation rate. Hesebeck (2000) showed that it is necessary to formulate the loading functions in the space of the dissipative forces to ensure the maximum dissipation rate. One problem is the often complex definition of the dissipative forces without clear physical meaning. To overcome this problem, the pseudo-logarithmic damage rate tensor, suggested by Carol et al. (2001a), is used in this approach.

Another essential topic in this framework is the localization problem. Several approaches have been proposed to overcome this problem: crack band approach, (Bažant, 1976), micropolar continua, (Cosserat and Cosserat, 2005), nonlocal models of the integral type, e.g. (Saouridis and Mazars, 1992) and gradient enhanced models, e.g. (Aifantis, 1984). Another class of approaches to overcome the localization phenomena introduces a discontinuity in the displacement field, see e.g. (Simo et al., 1993; Oliver, 1996).

In this paper, the crack band approach is applied, (Bažant, 1976; Bažant and Cedolin, 1980; Bažant and Oh, 1983); this approach is also often labeled as fracture energy approach. The basic idea is the modification of the material law in order to ensure always correct energy dissipation. This is reached by introducing a characteristic length in the constitutive law. In the literature, several approaches were suggested how to choose this characteristic length, see (Bažant and Oh, 1983; Rots, 1988; Oliver, 1989; Cervenka, 1995; Lackner, 1999; Winkler, 2001) or (Pölling, 2000). Simulations by using the range of suggested values for the characteristic length are performed in this paper, but the simulations overestimate the experimentally observed peak load considerably. Hence, the question is why these overestimations appear? One essential problem is that the characteristic length has no clear meaning.

The basic and new idea in this paper is that the characteristic length should always coincide with the width of the dissipative zone appearing in the simulation. The integration points with increasing damage in one loading increment are the dissipative zone in this loading increment. But the width of the dissipative zone is not known in advance. Simulations of a double edge notched specimen—experiment are performed in order to investigate the evolution of the dissipative zone for varying characteristic lengths. The investigations show that the width of the dissipative zone depends on the damage at the specific material point and the inclination angle between the damage direction and the element edges. An approach for the characteristic length to describe this relationship is suggested. A simulation by using this approach shows a sufficient coincidence of the characteristic length with the width of the dissipative zone and convincing results, like e.g. the load–displacement curve, are obtained. To evaluate the validity of the suggested theory, further simulations using a finer discretization are investigated. An influence of the element size on the width of the dissipative zone is observed. A modification of the approach for the characteristic length is necessary in order to attain the coincidence of the characteristic length with the width of the dissipative zone in the finer mesh. A simulation by using this modified approach with the fine mesh yields good coincidence and approximately the same results as the simulation with the coarse mesh and the first approach.

The paper is subdivided into two parts. The constitutive model is derived in Section 2 and the investigations concerning the characteristic length and the dissipative zone are performed in Section 3.

2. Description of the model

2.1. Damage operator, energy equivalence approach

The basis of this model is the definition of an effective, intact material, (Carol et al., 2001a; Lemaitre, 1991), with an effective stress σ_{ij}^{eff} and an effective strain $\epsilon_{ij}^{\text{eff}}$. The goal of this section is the derivation of a linear damage operator, which connects the effective material state to the nominal material state described by the nominal stress σ_{ij} and the nominal strain ϵ_{ij}. The relationship between these effective quantities is assumed to be linear elastic and isotropic with the stiffness E_{ijkl}^0:

$$\sigma_{ij}^{\text{eff}} = E_{ijkl}^0 \epsilon_{kl}^{\text{eff}}.$$

The constitutive law for the real, damaged material with the damaged stiffness E_{ijkl} being dependent on a general damage variable D_* is

$$\sigma_{ij} = E_{ijkl}(D_*, E_{ijkl}^0)\epsilon_{kl}. \tag{1}$$

The variable can be both a scalar and a tensor. The relationship between the nominal and the effective quantities is assumed to be linear. The damage operator is in the form of a fourth-order tensor based on the requirement that a second-order tensor remains a second-order tensor after a linear operation. Utilizing this fact, it is then possible to address approaches for stress and strain:

$$\sigma_{ij}^{\text{eff}} = A_{ijkl}\sigma_{kl}, \quad \epsilon_{ij}^{\text{eff}} = B_{ijkl}\epsilon_{kl}. \tag{2}$$

At this point, it can only be stated that the operators have the property of minor symmetry since σ_{ij} and ϵ_{ij} are symmetric. In order to proceed with the definition of the damage operator, a physical assumption is needed to connect the effective material to the actual material. The equivalence principles are such assumptions, see e.g. (Lemaitre, 1991). The energy equivalence approach is used because it ensures the symmetry of the secant stiffness as shown at the end of this section. This approach combines the actual material with the effective material based on the assumption that the accumulated elastic energy u is the same in both:

$$u = \frac{1}{2}\sigma_{ij}\epsilon_{ij} = \frac{1}{2}\sigma_{ij}^{\text{eff}}\epsilon_{ij}^{\text{eff}} = \frac{1}{2}A_{ijkl}\sigma_{kl}B_{ijrs}\epsilon_{rs}$$
$$u = \frac{1}{2}\boldsymbol{\sigma} : \boldsymbol{\epsilon} = \frac{1}{2}\boldsymbol{\sigma} : \mathbf{A}^T : \mathbf{B} : \boldsymbol{\epsilon}. \tag{3}$$

From this, it follows

$$\mathbf{A}^{\mathrm{T}} : \mathbf{B} = \mathbf{I}^4, \quad \mathbf{B} = \mathbf{A}^{-\mathrm{T}} \tag{4}$$

with the fourth-order identity tensor $\mathbf{I}^4$. With this, the relationship between **A** and **B** is derived by means of the equivalence principle. **A** is chosen as the linear damage operator. Thus, (2) can be rewritten as:

$$\sigma_{ij}^{\text{eff}} = A_{ijkl}(D_*)\sigma_{kl}, \quad \epsilon_{ij} = A_{klij}(D_*)\epsilon_{kl}^{\text{eff}}$$
$$\epsilon_{ij}^{\text{eff}} = \overline{A}_{klij}(D_*)\epsilon_{kl}, \quad \sigma_{ij} = \overline{A}_{ijkl}(D_*)\sigma_{kl}^{\text{eff}}$$

whereby, the inverse of **A** is named $\overline{\mathbf{A}}$. To formulate the operator **A** in detail, a convenient damage variable must be selected. In order to capture the load-induced anisotropy of concrete, the use of a second-order symmetric damage tensor D_{ij} is suggested, (Carol et al., 2001a) or (Lemaitre, 1991). This enables the modeling of orthotropic damage. Matrix representation of the tensor D_{ij} in the principal axes

$$[D_{ij}] = \begin{bmatrix} D_1 & 0 & 0 \\ 0 & D_2 & 0 \\ 0 & 0 & D_3 \end{bmatrix} \tag{5}$$

allows a comprehensive description of its meaning. The eigenvalues are defined as $0 \leqslant D_k < 1$ and $k = 1, 2, 3$; whereas, $D_k = 0$ represents intact material and $D_k \to 1$ completely destroyed material both in the direction of the eigenvector pertaining to D_k. However, it is advantageous for the formulation to use the integrity tensor $\bar{\phi}_{ij}$ in the model with the Kronecker delta δ_{ij}.

$$\bar{\phi}_{ij} = \delta_{ij} - D_{ij}.$$

Additionally, the inverse integrity tensor ϕ_{ij} and, for the sake of symmetry, the tensors $\bar{w}_{ij}$ and w_{ij} are introduced, (Carol et al., 2001a):

$$\bar{\phi}_{ij} = \bar{w}_{ik}\bar{w}_{kj}, \quad \phi_{ij} = w_{ik}w_{kj}$$
$$\bar{\phi}_{ik}\phi_{kj} = \phi_{ik}\bar{\phi}_{kj} = \delta_{ij}$$
$$\bar{w}_{ik}w_{kj} = w_{ik}\bar{w}_{kj} = \delta_{ij}.$$

The next step involves an approach for determining the damage operator **A** in one of these variables. The formulation used by Carol et al. (2001a) is chosen:

$$A_{ijkl} = \frac{1}{2}(w_{ik}w_{jl} + w_{il}w_{jk})$$

and

$$\overline{A}_{ijkl} = \frac{1}{2}(\bar{w}_{ik}\bar{w}_{jl} + \bar{w}_{il}\bar{w}_{jk}). \tag{6}$$

The nominal, secant constitutive law can be derived by the definition of **A**:

$$\sigma_{ij} = \overline{A}_{ijkl}\sigma_{kl}^{\text{eff}} = \overline{A}_{ijkl}E_{klmn}^0\epsilon_{mn}^{\text{eff}} = \overline{A}_{ijkl}E_{klmn}^0\overline{A}_{opmn}\epsilon_{op}. \tag{7}$$

Substituting (6) yields

$$\sigma_{ij} = \bar{w}_{ip}\bar{w}_{jq}\bar{w}_{kr}\bar{w}_{ls}E_{pqrs}^0\epsilon_{kl} \tag{8}$$
$$\boldsymbol{\sigma} = \mathbf{E}(\mathbf{E}^0, \mathbf{w}) : \boldsymbol{\epsilon} = \mathbf{E}(\mathbf{E}^0, \boldsymbol{\phi}) : \boldsymbol{\epsilon} \tag{9}$$

with the secant stiffness

$$E_{ijkl} = \bar{w}_{ip}\bar{w}_{jq}\bar{w}_{kr}\bar{w}_{ls}E_{pqrs}^0$$
$$\mathbf{E} = \Lambda_0\bar{\boldsymbol{\phi}} \otimes \bar{\boldsymbol{\phi}} + 2G_0\bar{\boldsymbol{\phi}}\underline{\otimes}\bar{\boldsymbol{\phi}} \tag{10}$$

and the elastic isotropic parameters Λ_0, G_0. The product $\underline{\otimes}$ means: $\mathbf{a}\underline{\otimes}\mathbf{a} = \frac{1}{2}(a_{ik}a_{jl} + a_{il}a_{jk})\mathbf{e}_i \otimes \mathbf{e}_j \otimes \mathbf{e}_k \otimes \mathbf{e}_l$. Finally, a remark on the symmetry of the secant stiffness: Equating (7) with (9) leads to

$$E_{ijkl} = \overline{A}_{ijmn}E_{mnop}^0\overline{A}_{klop} \tag{11}$$

and with $E_{mnop}^0 = E_{opmn}^0$ the major symmetry of the secant stiffness follows:

$$E_{ijkl} = \overline{A}_{ijmn}E_{opmn}^0\overline{A}_{klop} = \overline{A}_{klop}E_{opmn}^0\overline{A}_{ijmn} = E_{klij}.$$

2.2. Evolution rule, principle of maximum energy dissipation rate

The goal of this section is the derivation of an evolution rule for the damage, where $\boldsymbol{\phi}$ is the damage variable. With Eq. (9), the Helmholtz free energy results for elastic degrading material:

$$\rho_0\psi(\boldsymbol{\epsilon},\mathbf{E}) = \frac{1}{2}\boldsymbol{\epsilon} : \mathbf{E}(\mathbf{E}^0,\boldsymbol{\phi}) : \boldsymbol{\epsilon}.$$

The internal variables are $\boldsymbol{\epsilon}$ and $\boldsymbol{\phi}$, and the thermodynamically conjugate variables are $\boldsymbol{\sigma}$ and $\mathbf{Y}_\phi$:

$$\boldsymbol{\sigma} = \rho_0\frac{\partial\psi}{\partial\boldsymbol{\epsilon}} = \mathbf{E} : \boldsymbol{\epsilon}, \quad \mathbf{Y}_\phi = \rho_0\frac{\partial\psi}{\partial\boldsymbol{\phi}}.$$

The variable $\mathbf{Y}_\phi$ is also often designated as the dissipative force. The total differential is

$$\rho_0\dot{\psi} = \boldsymbol{\epsilon} : \mathbf{E} : \dot{\boldsymbol{\epsilon}} + \rho_0\frac{\partial\psi}{\partial\boldsymbol{\phi}} : \dot{\boldsymbol{\phi}}.$$

If this is inserted in the Clausius–Duhem inequality for isothermal processes,

$$\rho_0\dot{\psi} \leqslant \boldsymbol{\sigma} : \dot{\boldsymbol{\epsilon}},$$

then follows

$$0 \leqslant [\boldsymbol{\sigma} - \boldsymbol{\epsilon} : \mathbf{E}] : \dot{\boldsymbol{\epsilon}} - \rho_0\frac{\partial\psi}{\partial\boldsymbol{\phi}} : \dot{\boldsymbol{\phi}}$$

whereby, the dissipative portion P_{dis} of the process becomes clear as shown below:

$$P_{\text{dis}} = -\rho_0\frac{\partial\psi}{\partial\boldsymbol{\phi}} : \dot{\boldsymbol{\phi}} = -\mathbf{Y}_\phi : \dot{\boldsymbol{\phi}}.$$

In order to be able to work with a positive quantity, $-\mathbf{Y}_\phi$ is chosen as the dual variable to $\boldsymbol{\phi}$. The derivation of the evolution law is based on the physical assumption that a system tries to dissipate stored energy as quickly as possible. Hence, the energy dissipation rate P_{dis} is maximized. P_{dis} shall be maximized under the constraints of $\zeta_k = 0,\ k = 1,2,3$. The constraints ζ_k are the loading functions F_k, which distinguish elastic material response from progressive damage. The maximization is attained by converting the problem into a minimization problem which is solved by a Lagrange minimization of $-P_{\text{dis}}$, see e.g. (Luenberger, 1984). By introducing the Lagrange multipliers $\dot{\lambda}_k \geqslant 0$, the Lagrange function Ξ becomes

$$\Xi = -P_{\text{dis}} + \sum_{k=1}^{3}\dot{\lambda}_k\zeta_k = -(-\mathbf{Y}_\phi : \dot{\boldsymbol{\phi}}) + \sum_{k=1}^{3}\dot{\lambda}_k\zeta_k$$

and the minimization gives the evolution rule:

$$\begin{aligned}&\frac{\partial\Xi}{\partial(-\mathbf{Y}_\phi)} = 0 \rightarrow\\ &\dot{\boldsymbol{\phi}} = \sum_{k=1}^{3}\dot{\lambda}_k\frac{\partial\zeta_k}{\partial(-\mathbf{Y}_\phi)} = \sum_{k=1}^{3}\dot{\lambda}_k\frac{\partial F_k}{\partial(-\mathbf{Y}_\phi)}.\end{aligned} \tag{12}$$

The use of three loading functions F_1, F_2, F_3 enables the modeling of damage in three different directions in a decoupled way. These directions are defined by the eigenvectors of $-\mathbf{Y}_\phi$. If the loading function F_1 is active, the damage increases in the direction pertaining to the largest eigenvalue of $-\mathbf{Y}_\phi$. If F_2 is active, then the damage increases only in the direction of the second eigenvalue of $-\mathbf{Y}_\phi$ and the same analogously holds for the smallest eigenvalue of $-\mathbf{Y}_\phi$.

Given Eq. (12), the evolution rule applies for given loading functions F_k. At this point, the loading functions F_k are introduced as constraints; however, nothing is known about the variables constituting the loading functions. The following considerations suggest the definition $F_k(-\mathbf{Y}_\phi)$:

- The derivatives $\frac{\partial F_k}{\partial(-\mathbf{Y}_\phi)}$ must exist in order to fulfill the principle of maximum dissipation rate and to calculate the damage evolution $\dot{\boldsymbol{\phi}}$.
- The definition of $F(-\mathbf{Y}_\phi)$ together with the evolution rule in Eq. (12) ensure a symmetric tangent stiffness, (Carol et al., 1994); this is advantageous.

Furthermore, Eq. (12) constrains the freedom of the design of the loading functions. Rewriting Eq. (12) and (2) in the principal basis yields

$$\sum_{j=1}^{3}\dot{\phi}_j\mathbf{v}_j\otimes\mathbf{v}_j = \sum_{j=1}^{3}\sum_{k=1}^{3}\dot{\lambda}_k\frac{\partial F_k}{\partial(-Y_{\phi j})}\mathbf{v}_j\otimes\mathbf{v}_j \tag{13}$$

with the eigenvectors $\mathbf{v}_j$ of $-\mathbf{Y}_\phi$. Assuming only F_1 to be active and F_2, F_3 to be inactive simplifies this equation:

$$\sum_{j=1}^{3} \dot{\phi}_j \mathbf{v}_j \otimes \mathbf{v}_j = \sum_{j=1}^{3} \dot{\lambda}_1 \frac{\partial F_1}{\partial(-Y_{\phi,j})} \mathbf{v}_j \otimes \mathbf{v}_j. \tag{14}$$

Damage can only increase, which means

$$\dot{\phi}_1 > 0, \quad \dot{\phi}_2 > 0, \quad \dot{\phi}_3 > 0. \tag{15}$$

Using the positive definition of the Lagrange multipliers and considering Eq. (14) give the requirements

$$\frac{\partial F_1}{\partial(-Y_{\phi,1})} > 0, \quad \frac{\partial F_1}{\partial(-Y_{\phi,2})} > 0, \quad \frac{\partial F_1}{\partial(-Y_{\phi,3})} > 0 \tag{16}$$

based on Eq. (15). These equations have to be fulfilled by every formulation of a loading function F_1. The same requirements analogously hold for the loading functions F_2 and F_3.

2.3. Pseudo-log damage rate

In the last section the inverse ϕ_{ij} of the integrity tensor was defined as the damage variable and the conjugate quantity $-\mathbf{Y}_\phi$ was suggested to be a variable of the damage surfaces. Utilizing (Carol et al., 2001a), $-\mathbf{Y}_\phi = -\rho_0 \frac{\partial \psi}{\partial \phi}$ becomes

$$-Y^{\phi}_{pq} = \frac{-\nu^0}{E^0}(\sigma_{kl}\phi_{kl})\sigma_{pq} + \frac{1+\nu^0}{E^0}\sigma_{pk}\phi_{kl}\sigma_{lq} \tag{17}$$

with the Young's modulus E^0 and Poisson's ratio ν^0 of the intact, isotropic material. A physical meaning of $-Y^{\phi}_{pq}$ is, however, difficult to recognize and for this reason a definition of $F(-Y^{\phi}_{pq})$ is disadvantageous. Hence, the "pseudo-logarithmic damage tensor rate"

$$\dot{L}_{rs} = 2\bar{w}_{rp}\dot{\phi}_{pq}\bar{w}_{rs} \tag{18}$$

is introduced as a modified damage variable in Carol et al. (2001a), which is defined only as a rate tensor, in general. The advantage is found in the dual quantity of $\dot{L}_{ij}$, which is a simple and physically comprehensive quantity by which the loading surface is defined:

$$-Y_{ik} = \frac{1}{2}\sigma^{\text{eff}}_{ij}\epsilon^{\text{eff}}_{jk}.$$

The detailed derivation of $-Y_{ik}$ is given in Carol et al. (2001a). For example, the first invariant of $-Y_{ik}$ is the stored elastic energy. Transformation of $-Y_{ik}$ into the principal axes yields the energy-like, but direction-dependent quantities $-Y_\alpha$. The dissipation potential with these quantities is

$$P_{\text{dis}} = -Y_{ij}\dot{L}_{ij},$$

and maximization leads to the evolution rule for $\dot{L}_{ij}$:

$$\dot{L}_{ij} = \sum_{k=1}^{3} \dot{\lambda}_k \frac{\partial F_k}{(\partial - Y_{ij})}. \tag{19}$$

Additionally, Eq. (18) must be solved for $\dot{\phi}_{pq}$ for subsequent derivations.

$$\dot{\phi}_{pq} = \frac{1}{2} w_{pr}\dot{L}_{rs}w_{sq} \tag{20}$$

The introduced pseudo-log damage rate $\dot{L}_{rs}$ cannot be integrated over the time, see Eq.(18). This means that the current material state must be stored in another damage variable. The inverse ϕ_{ij} of the integrity tensor is chosen.

Hence, the pseudo-log damage rate $\dot{L}_{rs}$ can be seen as an auxiliary damage variable in rate-form. Its introduction enables a formulation with loading functions being defined in physically comprehensive variables.

2.4. Loading surfaces

A loading function must contain both a loading state descriptive component defined in $-Y_{ij}$ and a component describing the current material state. The material descriptive component must be defined in a variable that represents the damage of the material. In the previous section, the pseudo-log damage rate $\dot{L}_{ij}$ was chosen as damage variable, but the integral of $\dot{L}_{ij}$ over the time does generally not exist. Because the loading surface must be defined in a damage variable and not in a rate of a damage variable, ϕ_{ij} is used as the variable of the material descriptive component of the loading surfaces. Since this formulation is complicated due to its second-order tensor components, the loading functions are determined in the eigenvalues of $-Y_{ij}$ and ϕ_{ij}. This also enables a simple decoupling, and the proposed structure becomes:

$$F_1(-Y_1, \phi_1), F_2(-Y_2, \phi_2), F_3(-Y_3, \phi_3).$$

Because the subsequent derivations are the same for all three loading surfaces F_k, the determination of $F_1(-Y_1, \phi_1)$ is demonstrated only. Basically, the structure of F_1 is assumed to be

$$F_1(-Y_1, \phi_1) = f_1(-Y_1) - r_1(\phi_1) \tag{21}$$

if the loading portion is $f_1(-Y_1)$ and the material descriptive state is $r_1(\phi_1)$. For this approach, the following material-specific properties are assumed:

- Concrete reacts with energy dissipation only on tensile loadings. In this way $f_1(-Y_1)$ becomes $f_1(-\widehat{Y}_1)$ with

  $$-\widehat{Y}_1 = \frac{1}{2}\langle\sigma_1^{\text{eff}}\rangle\langle\epsilon_1^{\text{eff}}\rangle$$

  and the Mac Auley brackets $\langle\ldots\rangle$. The meaning of the Mac Auley brackets is $\langle x\rangle = x$, if $x > 0$ and $\langle x\rangle = 0$, if $x \leqslant 0$.
- In the uniaxial case, concrete has the ability to store added elastic energy up to a value of $u_t = \frac{1}{2}\frac{f_t^2}{E_0}$, with the mean tensile strength f_t. Once the value of u_t is exceeded the concrete responds by dissipating a portion of the additional energy through the formation of crack surfaces. In the uniaxial tension case $-\widehat{Y}_1 = \frac{1}{2}\frac{f_t^2}{E_0}$ is valid at the elastic boundary whereby the following form of $f(-\widehat{Y}_1)$ is suitable:

  $$f_1(-\widehat{Y}_1) = -\widehat{Y}_1.$$

Based on these assumptions, Eq. (21) becomes

$$F_1(-\widehat{Y}_1, \phi_1) = -\widehat{Y}_1 - r_1(\phi_1). \tag{22}$$

Carol et al. (2001b) suggested a similar, but coupled formulation.

The derivation of a damage evolution $r_1(\phi_1)$ is the next step. This approach is based on the requirement that the actual physical behavior of normal concrete be simulated in uniaxial tension; in particular, the same amount of energy must be dissipated in the simulation as in the experiment. For the uniaxial tensile case, the equations

$$\sigma_1^{\text{eff}} = \sigma_1\phi_1, \quad \epsilon_1^{\text{eff}} = \frac{\epsilon_1}{\phi_1}$$

are valid and the loading function in the case of progressive damage is:

$$F_1 = -\widehat{Y}_1 - r(\phi_1) = \frac{1}{2}\sigma_1\epsilon_1 - r_1(\phi_1) = 0. \tag{23}$$

Next, an approach for $\sigma_1(\epsilon_1)$ is formulated for σ_1 in Eq. (23) that models the tensile behavior of normal concrete. The first step is a modification of the stress-crack opening relationship suggested by Gopalaratnam and Shah (1985):

$$\sigma_1 = f_t e^{-kw} \tag{24}$$

with the crack opening w in $[m]$ and a parameter k. Assuming a maximum crack opening of $w_c = 0.15$ mm, at which stress can no longer be transferred, enables the determination of k for a given fracture energy G_f and a tensile strength f_t:

$$G_f = \int_0^{w_c}\sigma_1 dw = \int_o^{w_c} f_t e^{-kw} dw. \tag{25}$$

Therewith, the fracture energy is implicitly captured by k. Hence, the fracture energy G_f appears no longer in the following formulations. In order to obtain a stress–strain law, the crack opening w must be related to a width h_{ch}, which is the assumed width of the dissipative zone. The width h_{ch} is the characteristic length embedded into the constitutive model and must be carefully chosen to regularize a simulation. The lower index ch represents the word *chosen*:

$$\sigma_1 = f_t e^{-k\epsilon_1\cdot h_{ch}}.$$

Furthermore, taking into account the fact that softening is not supposed to begin before the tensile strength is reached yields:

$$\sigma_1 = f_t e^{-k(\epsilon_1 - f_t/E_0)\cdot h_{ch}}. \tag{26}$$

With this, the relationship $\sigma_1(\epsilon_1)$ for Eq. (23) is given. Applying the uniaxial tensile conditions to Eq. (8) results in:

$$\sigma_1 = \frac{E_0}{\phi_1^2}\epsilon_1. \tag{27}$$

Comparing Eq. (27) with Eq. (26) and solving for ϵ_1 provides

$$\epsilon_1(\phi_1) = \frac{1}{kh_{ch}} W\left(\frac{kh_{ch}f_t\phi_1^2 e^{\frac{kh_{ch}f_t}{E_0}}}{E_0}\right)$$

using the Lambert function $W(..)$. Given a function $y = xe^x$, the Lambert function is the inverse function $x = W(y)$. Inserting $\epsilon_1(\phi_1)$ into Eq. (26) yields the expression $\sigma_1(\phi_1)$. To obtain the formulation of the damage evolution $r_1(\phi_1)$, the expressions $\epsilon_1(\phi_1)$ and $\sigma_1(\phi_1)$ need only be employed in Eq. (23). This provides the damage evolution

$$r_1(\phi_1) = \frac{1}{2}\sigma_1(\phi_1)\epsilon_1(\phi_1) = \frac{0.5}{kh_{\mathrm{ch}}} V_1 f_{\mathrm{t}} \mathrm{e}^{\left(-k\left(\frac{1}{kh_{\mathrm{ch}}}V_1 - \frac{f_{\mathrm{t}}}{E_0}\right)h_{\mathrm{ch}}\right)}$$

with $Z = \mathrm{e}^{(\frac{kh_{\mathrm{ch}}f_{\mathrm{t}}}{E_0})}$ and $V_1 = W(\frac{kh_{\mathrm{ch}}f_{\mathrm{t}}\phi_1^2 Z}{E_0})$. Inserting $r_1(\phi_1)$ into Eq. (22) and parallel procedures for the surfaces F_2 and F_3 yield the three sought-after loading functions:

$$F_k(-\widehat{Y}_k, \phi_k) = -\widehat{Y}_k - \frac{0.5}{kh_{\mathrm{ch}}} V_k f_{\mathrm{t}} \mathrm{e}^{\left(-k\left(\frac{1}{kh_{\mathrm{ch}}}V_k - \frac{f_{\mathrm{t}}}{E_0}\right)h_{\mathrm{ch}}\right)}. \tag{28}$$

2.5. Final system of constitutive equations

The complete material law consists of the secant constitutive law

$$\boldsymbol{\sigma} = \mathbf{E}(\mathbf{E}^0, \boldsymbol{\phi}) : \boldsymbol{\epsilon}, \quad \mathbf{E}(\mathbf{E}^0, \boldsymbol{\phi}) = \Lambda_0 \vec{\boldsymbol{\phi}} \otimes \vec{\boldsymbol{\phi}} + 2G_0 \vec{\boldsymbol{\phi}} \underline{\boxtimes} \vec{\boldsymbol{\phi}},$$

the evolution laws

$$\dot{\boldsymbol{\phi}} = \frac{1}{2}\mathbf{w} \cdot \dot{\mathbf{L}} \cdot \mathbf{w}, \quad \dot{\mathbf{L}} = \sum_{k=1}^{3} \dot{\lambda}_k \frac{\partial F_k}{(\partial - \mathbf{Y})} \tag{29}$$

and the loading functions

$$F_k(-\widehat{Y}_k, \phi_k) = -\widehat{Y}_k - \frac{0.5}{kh_{\mathrm{ch}}} V_k f_{\mathrm{t}} \mathrm{e}^{\left(-k\left(\frac{1}{kh_{\mathrm{ch}}}V_k - \frac{f_{\mathrm{t}}}{E_0}\right)h_{\mathrm{ch}}\right)}. \tag{30}$$

The final system of constitutive equations is solved by a Newton–Raphson-method, represented in detail in Pröchtel and Häußler-Combe (2007), and then implemented into an FE-code being developed at the institute.

3. Localization analysis

Concrete is a heterogeneous material, which shows under tensile loading the appearance and especially the coalescence of microcracks leading to a concentration of defects in a process zone. This behavior results in discontinuities appearing in the strain rates of the mechanical field. Investigations about the onset of such discontinuities were performed by e.g. (Rizzi et al., 1996) inspired by the early work of Hill (1958).

Another very important topic in localization analysis is the evolution of the localization during a simulation. This is a rather new field and some investigations were performed by, e.g. (Patzák and Jirasék, 2002, Grassl and Jirasék, 2005). In these studies, nonlocal continuum approaches and extended finite elements were applied to regularize the simulations.

In this paper, the evolution of the localization, which is equal to the evolution of the dissipative zone, is investigated by applying the crack band approach as the regularization technique. The study is based on a structural application and not on basic uniaxial considerations.

In Section 2.4, the necessity was mentioned to choose the characteristic length embedded in the constitutive model h_{ch} carefully to regularize a simulation. The essential point is to ensure that the dissipated energy matches in simulation and experiment. This holds true for both a complete system and a local part of the process zone. The new idea in this paper is that the chosen parameter h_{ch} should be always equal to the width of the energy-dissipating zone that appears in a simulation in order to attain the correct energy dissipation. The width of the dissipative zone that appears in the simulation has the name h_{sim}, the lower index sim represents the word *simulation*.

Other models that use the fracture energy approach to regularize are e.g. smeared crack models, (Rots, 1988; Oliver, 1989; Cervenka, 1995), plastic models, (Winkler, 2001; Lackner, 1999) or anisotropic damage models, (Pölling, 2000). An usual approach is to choose h_{ch} as the square root of the element area. Enhancements that take into account the element geometry and the inclination of the crack to the element edges are also applied. The important feature is that the width h_{ch} is assumed to be constant over the loading history.

3.1. Double-edge notched specimen

A standard experiment, the double-edge notched specimen experiment of Nooru-Mohamed (1992), was simulated to investigate the evolution of the dissipative zone and to test the validity of the mentioned values for h_{ch} from the literature. Based on the observations in the evolution of the dissipative zone, a new formulation for the characteristic length is suggested that fulfills the requirement that the characteristic length coincides with the width of the dissipative zone h_{sim}. In a first study, the dissipative zone was examined for a variety of chosen h_{ch}.

The geometry of the specimen is shown in Fig. 1. Steel plates were attached to simulate the load introduction as uniformly as possible. Compared to the experimental setup, additional steel plates were attached at the lower left and upper right sides of the concrete specimen. These plates were necessary due to load introduction problems experienced at the lower left and upper right-hand corners of the concrete specimen. The steel had a high Young's modulus in the simulations in order to capture the much larger dimensions of the steel frame in the experiment. The chosen material parameters of the concrete were $E_0 = 30000\ \mathrm{N/mm^2}, \nu = 0.2, f_t = 3.0\ \mathrm{N/mm^2}$ and $G_f = 110\ \mathrm{N/m}$. Inserting the parameters into Eq. (25) and solving for k yields $k = 26781.8/\mathrm{m}$. The specimen was loaded following load path 4B in Nooru-Mohamed (1992).

In the first step, the shear load F was applied by dividing it into two single loads. In the second step, the force F was held constant while the displacements u were applied. The loading in the first step was subdivided in one hundred increments and the second step in one thousand increments. The sum of the resulting forces, corresponding to prescribed displacements u, is labeled with P. Fig. 2 shows the range of the experimentally observed load–displacement curves and the observed crack pattern.

The following investigation on the evolution of the width of the dissipative zone is performed by a discretization with quadrilateral elements with four nodes and a plane stress case is assumed. In the center part of the model, the discretization is finer and regular, and the length of an element is $l_e = 0.0025\mathrm{m}$. In the following four simulations, the discretization is fixed. The parameter h_{ch} is changed and subsequently 1, 2, 3 and 4 times the element size.

First, a calculation with h_{ch} chosen as $h_{ch} = 0.0025$ m, which is equal to one element length, was performed. At this point, it must be stated that this simple choice is currently an often used approach. The existing, more advanced approaches use values for h_{ch} that take into account the inclination of the cracks to the element edges, (Rots, 1988; Oliver, 1989; Cervenka, 1995; Lackner, 1999). In these approaches, the chosen values for h_{ch} range between one element length and approximately two times the element length, both in the case of square elements.

In all following simulations, there was always only one damage surface active which means always $\phi_2 = \phi_3 = 1$ at every integration point. This enabled the representation of the damage at every integration point by a line that is oriented in the direction of the eigenvector according to eigenvalue ϕ_1 of $\boldsymbol{\phi}$ and the length of the line reflects the eigenvalue ϕ_1. Fig. 3(b) shows the final damage path of the first simulation with $h_{ch} = 0.0025$ m. The overlapping damaged zones conform to the

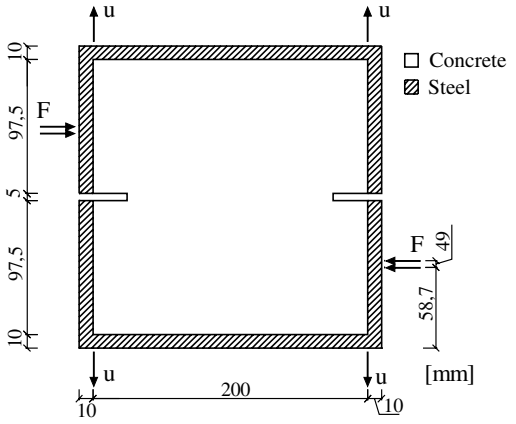

Fig. 1. Geometry of the double egde notched specimen.

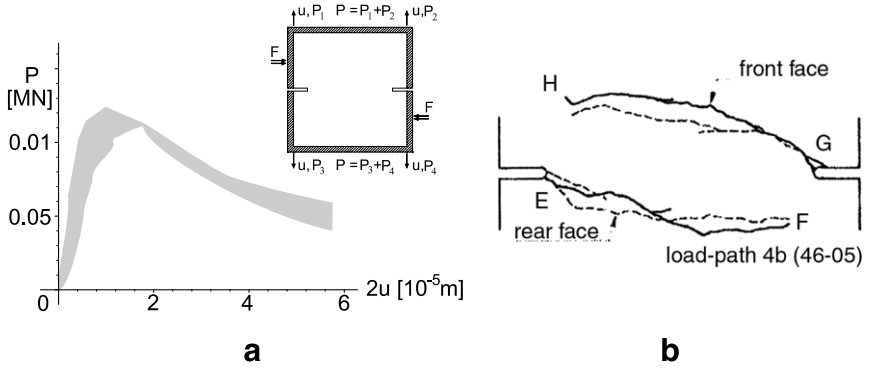

Fig. 2. (a) Experimentally observed load–displacement curves, (b) observed crack pattern (Nooru-Mohamed, 1992).

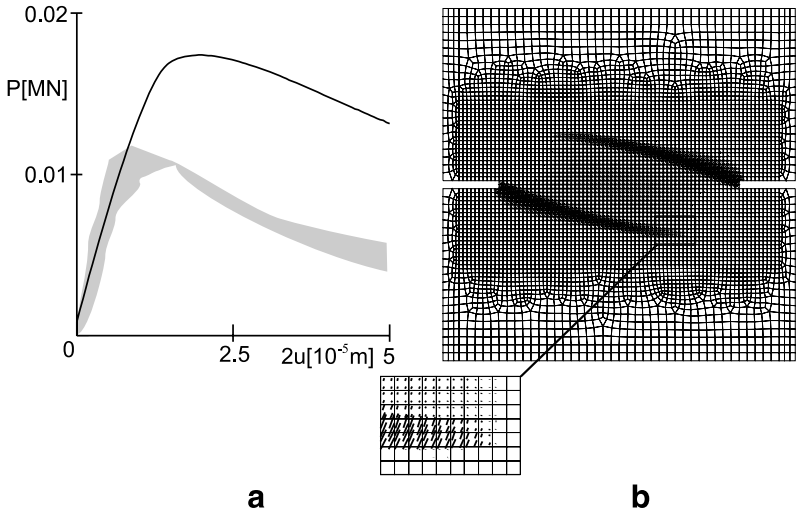

Fig. 3. Load–displacement curve (a) and damage path (b) at the displacement $2u = 5 \cdot 10^{-5}$ m, both for $h_{ch} = 0.0025$ m.

experimentally observed macro-cracks and their symmetry is correct, too. However, the area between the overlapping damaged zones is also slightly damaged although that could not be observed in the experiments. Fig. 3(a) shows the resulting load–displacement curves; the experimental results are shown in gray. The simulation overestimates the experimentally observed peak load considerably. Comparing the width of the simulated damage to the chosen width h_{ch} shows that they do not coincide. The width of the dissipative zone was assumed to be one length of an element, but the width of the damaged zone seems to be much wider.

This comparison is not correct, because we must distinguish the final damaged zone from the dissipative zone. The final damaged zone in Fig. 3(b) corresponds to the experimentally observed macrocracks at the prescribed displacement $u = 0.00005$ m. But the dissipative zone is the damage rate path. It is important to distinguish the damage path (damaged zone) from the damage rate path (dissipative zone). The damage rate path is the volume in the specimen where energy is dissipated in one specific loading situation, i.e. in one incremental step in the loading history. Energy dissipation occurs at these integration points, where the damage increases in the incremental step. Hence, one basic idea in this paper is that the range of the integration points with increasing damage must be considered in every of the 1100 incremental steps.

In order to attain correct energy dissipation, the width of this range, i.e. of the damage rate path, in damage direction should always have the same value as h_{ch} at every point and is labeled as h_{sim}. Hence, one of the main goals of the following investigations is the comparison of the characteristic length h_{ch} in the constitutive law to the width h_{sim} of the dissipative zone emerging in the simulation. Because it is impossible to compare them in all increments, only four characteristic loading situations are considered.

Fig. 4 shows the dissipative zone for four different loading situations in the magnification of the finer discretized part of the mesh: approximately 60% of the peak load (a); shortly before reaching the peak load (b); shortly after reaching the peak load (c) and one situation well into the softening regime (d). In the magnification of a small part of the dissipative zone, the measurement of the width h_{sim} is exemplarily presented in Fig. 4. The integration points with increasing damage are marked with points. In (a), the dissipative zone is much wider at the tip than one element length and the width decreases with increasing distance from the tip. Figures (b), (c) and (d) show that the width h_{sim} is decreasing over the loading history. Note that a constant width h_{ch} of one element length was assumed. However, this seems only to be a reasonable assumption in loading situation (d); all other Figures show a much wider dissipative zone. Obviously, the choice for h_{ch} as one element length is not correct.

In the second simulation, the width h_{ch} was chosen as $h_{ch} = 0.005$ m, which is equal to twice the element length. The resulting load–displacement curve and the damage path are shown in Fig. 5. The experimental peak load is still overestimated compared to the experiments but clearly less in comparison to Fig. 3(a). The damage paths conform to the experiments and the coupling effect between the overlapping damage paths that was observed in the last simulation is reduced. The damage path is more slender and more curved compared to the previous simulation. Fig. 6 again shows the dissipative zone for the four loading situations and the following can be observed:

- The width of the dissipative zone decreases over the loading history.
- The chosen $h_{ch} = 0.005$ m is too small for the situations (a) and (b), especially at the tip in situation (b). For the last two, it is relatively reasonable.
- A comparison of similar loading situations in the Figs. 4 and 6 shows smaller widths in Fig. 6 for all loading situations.

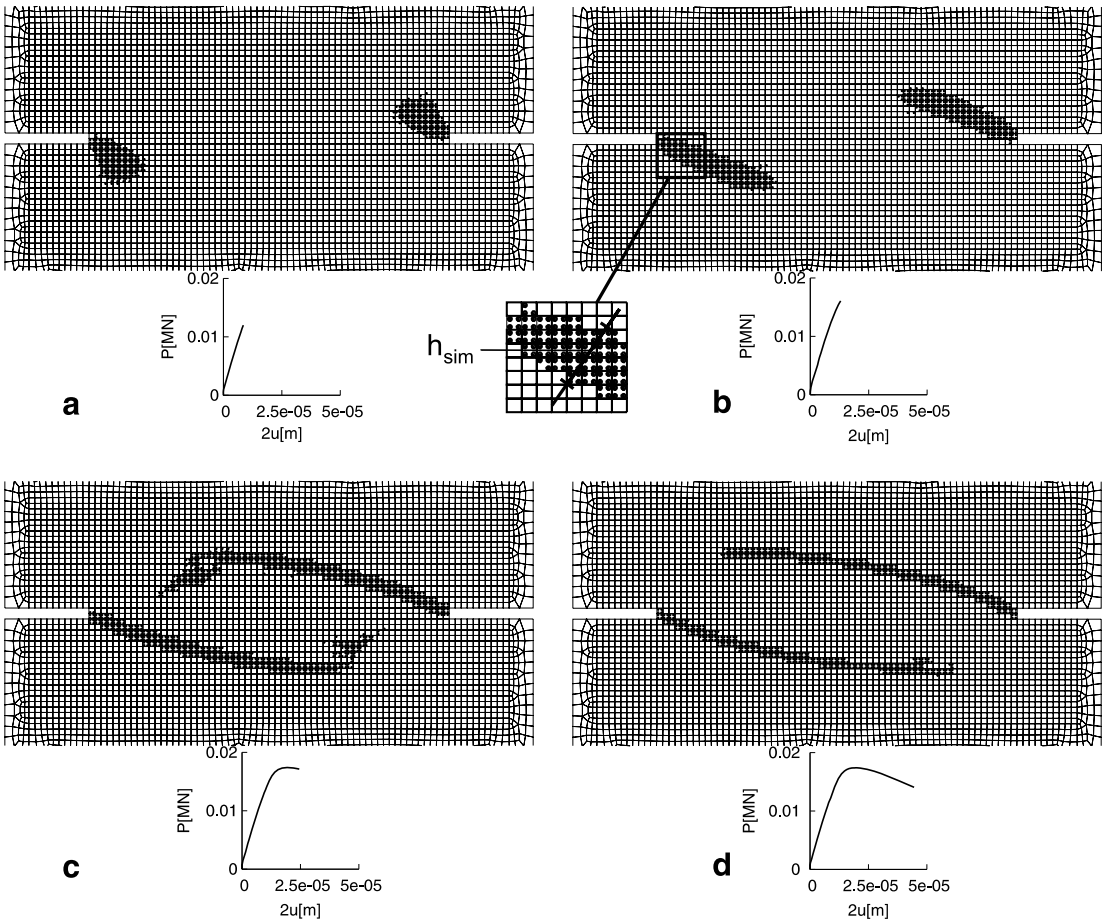

Fig. 4. Evolution of the damage rate path (dissipative zone) for $h_{ch} = 0.0025$ m.

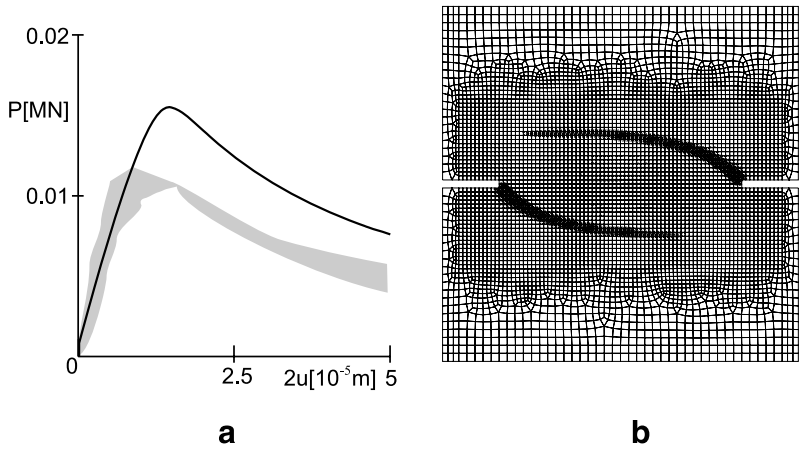

Fig. 5. Load–displacement curve (a) and damage path (b) at the displacement $2u = 5 \cdot 10^{-5}$ m, both for $h_{ch} = 0.005$ m.

- A relationship between the width h_{sim} and the angle of inclination of the damage path to the element edges can be seen in Fig. 6(d) where the material is progressively damaged. The width increases with increasing angle. This phenomenon is known from smeared cracks analysis (Rots, 1988; Oliver, 1989).
- Fig. 6(a) and (b) show that the width of the dissipative zone seems to decrease with increasing distance from the tip of the damage path. To realize that, it must be taken into account that the width also decreases with decreasing inclination of the damage path to the element edges.

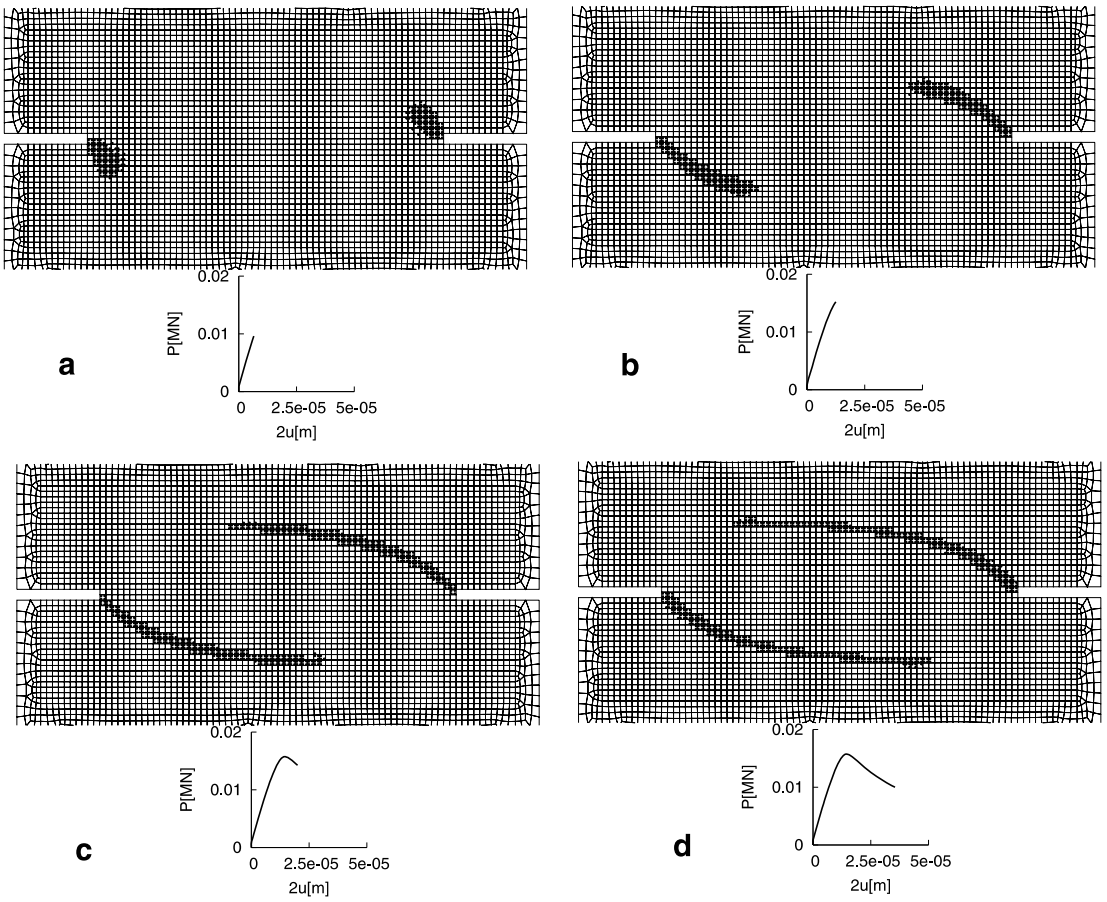

Fig. 6. Evolution of the damage rate path (dissipative zone) for $h_{ch} = 0.005$ m.

The two investigated simulations with $h_{ch} = l_e$ and $h_{ch} = 2l_e$ represent the range of suggested valued for h_{ch} in the literature, (Rots, 1988; Oliver, 1989; Cervenka, 1995; Lackner, 1999). In both simulations, the peak load is drastically overestimated and h_{sim} is generally too wide in comparison to h_{ch}.

In Fig. 7, the load-displacement curve and the damage path is represented for $h_{ch} = 0.0075$ m. The experimental peak load is overestimated by approximately 20%; this is an acceptable result in engineering applications. The slope of the curve after the peak load is slightly too steep. The slenderness and curvature of the damage paths continue increasing, and the unrealistic coupling effect between the overlapping damage paths almost disappears. Fig. 8 shows the dissipative zone; the same characteristics can be observed as in the previous simulations: the decrease of h_{sim} over the loading history; the increasing slenderness of the damage paths with increasing chosen h_{ch}; the increase of h_{sim} with increasing angle between the damage path and the element edges and the decrease of h_{sim} with increasing distance from the tip of the damage path.

Regarding the question about the correlation between h_{ch} and h_{sim}, the following can be observed: The choice of h_{ch} with three times the element length seems reasonable up to the peak load, h_{sim} is only a bit too wide. With larger distance from the tip, this choice is too large in Fig. 8(b). Regarding the softening regime, Fig. 8(c)–(d) always show a smaller h_{sim} than h_{ch}. This is the reason of the too stiff slope in the load–displacement curve after the peak load.

In the last simulation, the assumed width was chosen as $h_{ch} = 0.01$ m. The resulting load–displacement curve and the damage path are represented in Fig. 9. The simulated and the experimental peak load correspond well, but the slope of the curve is again too stiff after the peak load. The curvature and slenderness of the damage paths are similar to the previous simulation and the coupling effect vanished. Fig. 10 exhibits the same characteristics that were observed in the previous simulations related to the evolution of the dissipative zone. The correlation between h_{ch} and h_{sim} is similar to Fig. 8. Near the tip of the damage rate path in Fig. 10(a) and (b), the width h_{sim} corresponds well with h_{ch}, even better than in Fig. 8. But with larger distance from the tip and in Fig. 10(c) and (d), h_{sim} is too small.

The foregoing simulations had two main goals. The first was an investigation on the evolution of the dissipative zone. The second goal was to examine the coincidence of the chosen width h_{ch} and the observed one h_{sim}. Some basic features were observed:

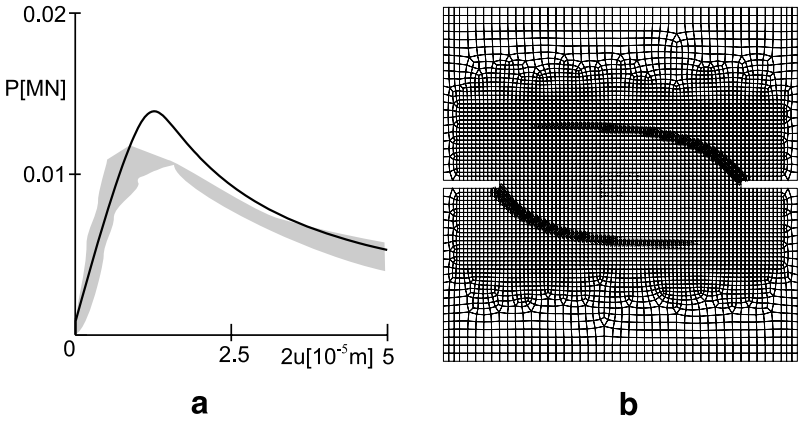

Fig. 7. Load–displacement curve (a) and damage path (b) at the displacement $2u = 5 \cdot 10^{-5}$ m, both for $h_{ch} = 0.0075$ m.

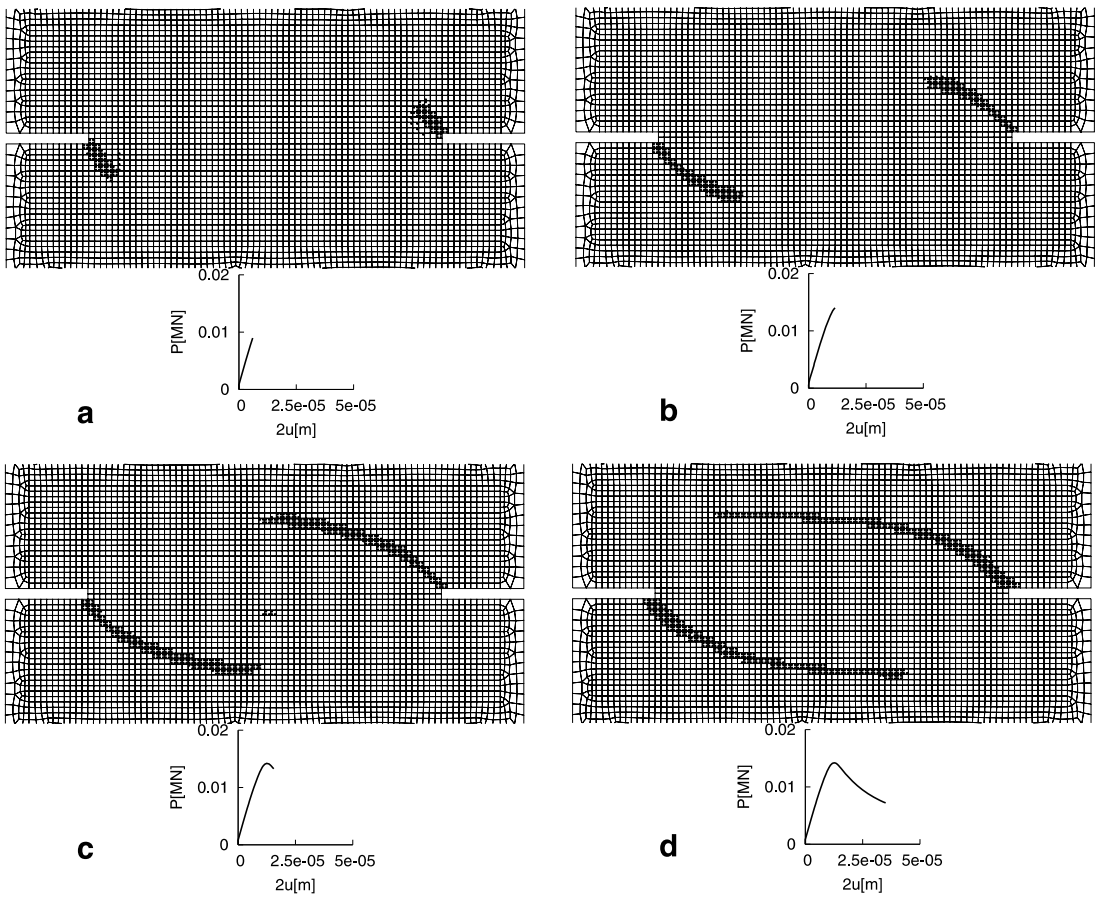

Fig. 8. Evolution of the damage rate path (dissipative zone) for $h_{ch} = 0.0075$ m.

- The smaller the chosen width h_{ch} is, the wider is the width h_{sim} of the dissipative zone in the simulations. Their development is opposite. Hence, in each loading situation exists only one value for h_{ch} that fulfills the requirement that h_{sim} equals h_{ch}.
- The width h_{sim} decreases with increasing distance from the tip of the damage path. Because the damage increases with increasing distance from the tip, it follows that the width h_{sim} decreases with increasing damage at the specific material point. This corresponds to experimental observations where the width of the process zone is also decreasing for increasing damage.
- The width h_{sim} increases with increasing angle between the damage path and the element edges.

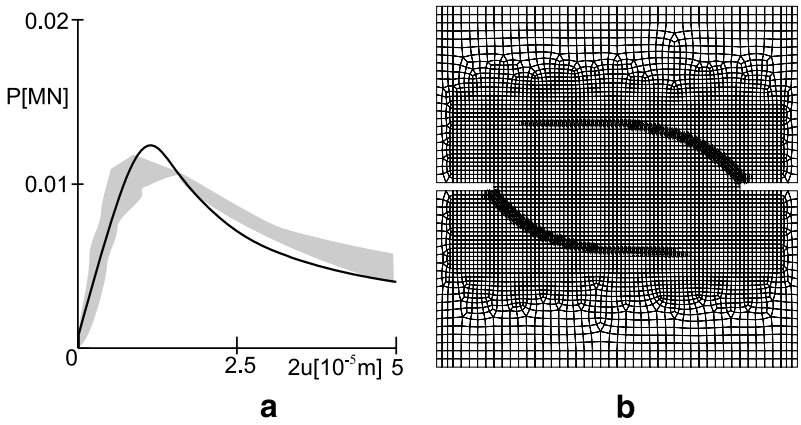

Fig. 9. Load–displacement curve (a) and damage path (b) at the displacement $2u = 5 \cdot 10^{-5}$ m, both for $h_{\mathrm{ch}} = 0.01$ m.

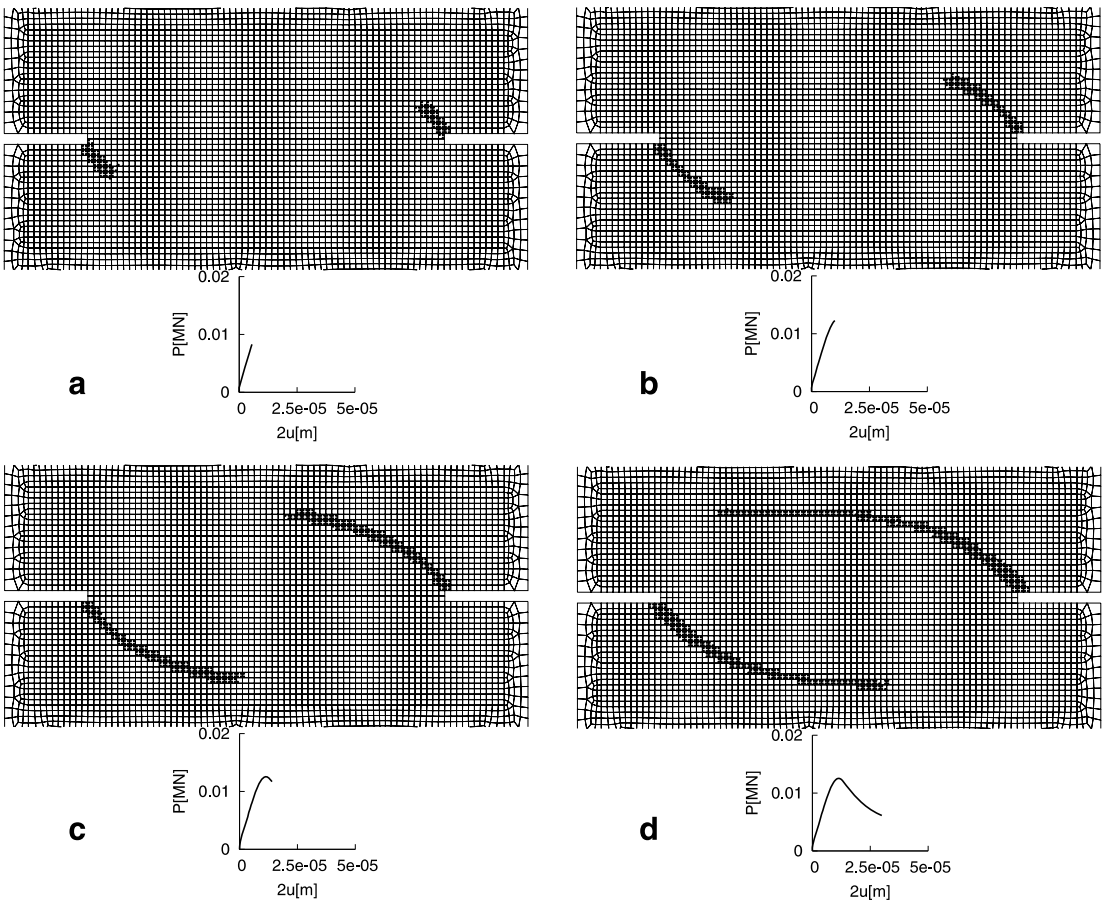

Fig. 10. Evolution of the damage rate path (dissipative zone) for $h_{\mathrm{ch}} = 0.01$ m.

During the calculation in the pre-peak regime, i.e., the damage rate path was curved, the best coincidence of h_{ch} and h_{sim} of the damage rate path was observed in Fig. 10(a) and (b), especially close to the tip of the damage rate path. The horizontal parts of the damage rate path in Figs. 6(d), 8(d) and 10(d) always show the same characteristics. The width h_{sim} amounts two times the element length close to the tip and $h_{\mathrm{sim}} \approx 1 \cdot l_e$ holds with larger distance from the tip.

Basing on the features concerning the evolution of the dissipative zone, it seems not appropriate to use a constant value h_{ch} over the complete loading history. The width of the dissipative zone seems to depend at least on the damage ϕ_1 at the

specific material point and the angle between the damage path and the element edges. At the specific material point, the angle α_1 between the eigenvector corresponding to the eigenvalue ϕ_1 and the element edges is used. The element edge giving the smaller angle is used, which means that $0 \leqslant \alpha_1 \leqslant \pi/4$ holds. This yields the basic approach

$$h_{\mathrm{ch},1}(\bar{\phi}_1, \alpha_1). \tag{31}$$

In a first basic approach, a bilinear relationship

$$h_{\mathrm{ch},1}(\bar{\phi}_1, \alpha_1) = a_1 + a_2 \cdot \bar{\phi}_1 + a_3 \cdot \alpha_1 + a_4 \cdot \bar{\phi}_1 \cdot \alpha_1 \tag{32}$$

is assumed. To determine the four parameters a_1, a_2, a_3, a_4, four boundary conditions are necessary. The goal of the following considerations is the formulation of these boundary conditions.

First, the curved sections of a damage path are considered and after that the sections where the damage path is approximately parallel to the element edges. The previous simulation with $h_{\mathrm{ch}} = 0.01\mathrm{m}$ is used for the curved regime because the width h_{sim} approximately corresponds with $h_{\mathrm{ch}} = 0.01\mathrm{m}$ close to the tip of the damage rate path. To get more insight in the structure of the dissipative zone in a curved section, Fig. 10(b) is replotted with additional information.

Besides the dissipative zone, the current damage value is plotted at every integration point in Fig. 11. The damage at every integration point is represented by the value $\bar{\phi}_1 = 1/\phi_1$. This is more convenient than plotting directly ϕ_1 because the values of ϕ_1 can be very large for progressive damage and the value of $\bar{\phi}_1$ tends to zero in this case. If the material is intact, then it holds $\bar{\phi}_1 = 1$. In Fig. 10(b) the integration points with increasing damage were marked with points. However, in Fig. 11 they are marked by underlining the damage value.

The magnification in Fig. 11 shows a much wider damaged zone than the dissipative zone, they only conform close to the tip. It can be realized that the damage value $\bar{\phi}_1$ is not constant over the width of the damaged zone. It is a distribution of the damage with a concentration in the central part and less damage at the margins of the damage path. Important for the approach in Eq. (31) is the damage $\bar{\phi}_1$ in the dissipative zone. The damage is distributed over the width h_{sim} of the dissipative zone, too. For further considerations, the estimated mean value over the width is used.

The assumption that h_{sim} decreases with increasing damage can be observed in Fig. 11. The width amounts approximately four times the element length close to the tip. With increasing distance from the tip of the damage path, the width is decreasing up to a width of approximately $h_{\mathrm{sim}} \approx 2.5 \cdot l_e$ when a mean value of $\bar{\phi}_1 \approx 0.4$ is attained in the dissipative zone. The inclination angle of the damage to the element edges is approximately $\alpha_1 = \pi/6$. With these considerations of curved sections of the damage path, two boundary conditions are given

- for intact material with a curved path $h_{\mathrm{ch},1}(\bar{\phi}_1 = 1, \alpha_1 = \pi/6) = 3.5 \cdot l_e$ and
- for damaged material with a curved path $h_{\mathrm{ch},1}(\bar{\phi}_1 = 0.4, \alpha_1 = \pi/6) = 2.5 \cdot l_e$.

More information about the dissipative zone in the horizontal part of a damage path are given by Fig. 8(d). The magnification is given in Fig. 12(a). Close to the tip of the damage path, the width has the value $h_{sim} \approx 2 \cdot l_e$ and some elements behind the tip, the width is $h_{sim} \approx 1 \cdot l_e$. The width $h_{sim} \approx 1 \cdot l_e$ is attained when the damage is $\bar{\phi}_1 \approx 0.4$. Fig. 12(b) shows the vector representation of the damage at every integration point in the same loading situation. Obviously, the vectors are not vertical. Their inclination angle to the element edges is approximately $\alpha_1 \approx \pi/18$. Therewith, the last two boundary conditions to determine the parameters in Eq. (32) are given

- for intact material with a horizontal damage path $h_{\mathrm{ch},1}(\bar{\phi}_1 = 1, \alpha_1 = \pi/18) = 2 \cdot l_e$ and
- for damaged material with a horizontal path $h_{\mathrm{ch},1}(\bar{\phi}_1 = 0.4, \alpha_1 = \pi/18) = 1 \cdot l_e$.

Using the boundary conditions and solving Eq. (32) for $a_1..a_4$ yields

$$h_{\mathrm{ch},1}(\bar{\phi}_1, \alpha_1) = (-0.4167 + 1.67 \cdot \bar{\phi}_1 + 4.297 \cdot \alpha_1) l_e, \tag{33}$$

with the restriction that, at any stage, $h_{\mathrm{ch},1} \geqslant l_e$ holds. The results of a simulation by applying this approach show the Figs. 13 and 14. The experimental peak load is overestimated by approximately 10%; this is an acceptable result in engineering applications. The comparison of the suggested approach $h_{\mathrm{ch},1}(\bar{\phi}_1, \alpha_1)$ with the width of the simulated dissipative zone shows a good agreement. This coincidence yields also a slope of the curve in Fig. 13(a) after the peak load which corresponds to the experiments.

The previous investigations showed how the choice of h_{ch} influences the dissipative zone appearing in the simulation. The widths h_{ch} and h_{sim} should coincide as good as possible. To attain that, the relationship in Eq. (33) was suggested. But it is clear that this is only a rough estimation. If e.g. the assumed value is $h_{\mathrm{ch},1} = 3.5 l_e$ at a specific material point, then the simulated width should be in the interval $h_{sim} \approx 3l_e \ldots 4l_e$. A more exact coincidence in all material points along the damage rate path is not possible.

Up to now, one discretization was performed only. The next step to evaluate the validity of the suggested theory and the approach $h_{\mathrm{ch},1}$, is to apply another discretization. A finer discretization is used and shown in Fig. 15. The length of the square elements in the refined part is $l_e = 0.00125$ m. The results of a simulation applying the $h_{\mathrm{ch},1}$-approach show the Figs. 16 and 17.

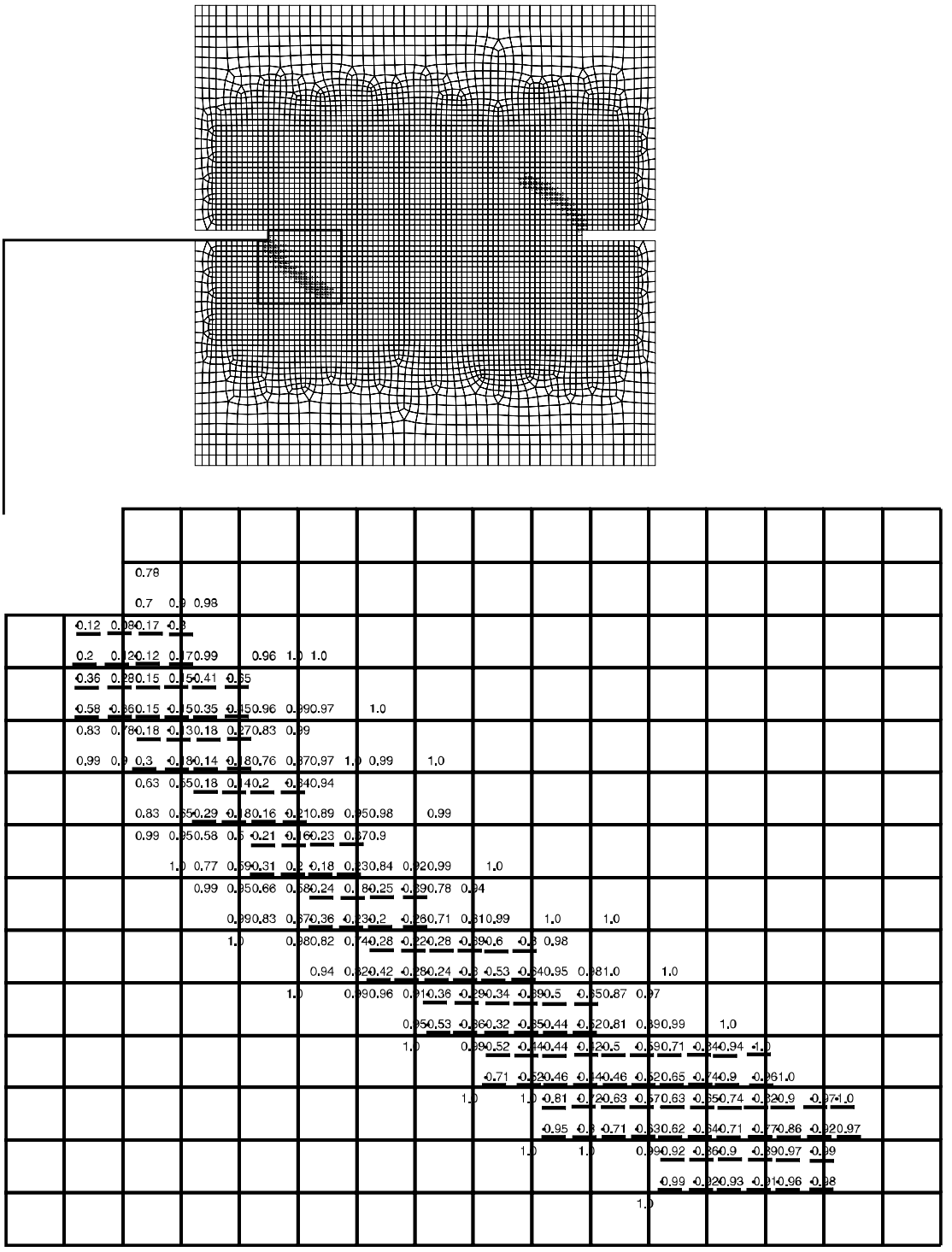

Fig. 11. Dissipative zone and damage values $\bar{\phi}_1$ in Fig. 10b.

The overestimation of the peak load increased in comparison to the results of the coarse mesh in Fig. 13(a). The damage rate path in Fig. 17 shows the same characteristics as in the coarse mesh. But, the width h_{sim} seems to be generally a bit too wide. This is particularly good to realize in sections that are relatively close to the tip of the path in the curved regime. When comparing the damage rate path in Fig. 17 to the path in Fig. 14, the width h_{sim} seems to be always $0.5l_e$—$1.0l_e$ wider in the fine mesh. This is an important observation, because it means that the width of the dissipative zone in a simulation depends on the element size, too.

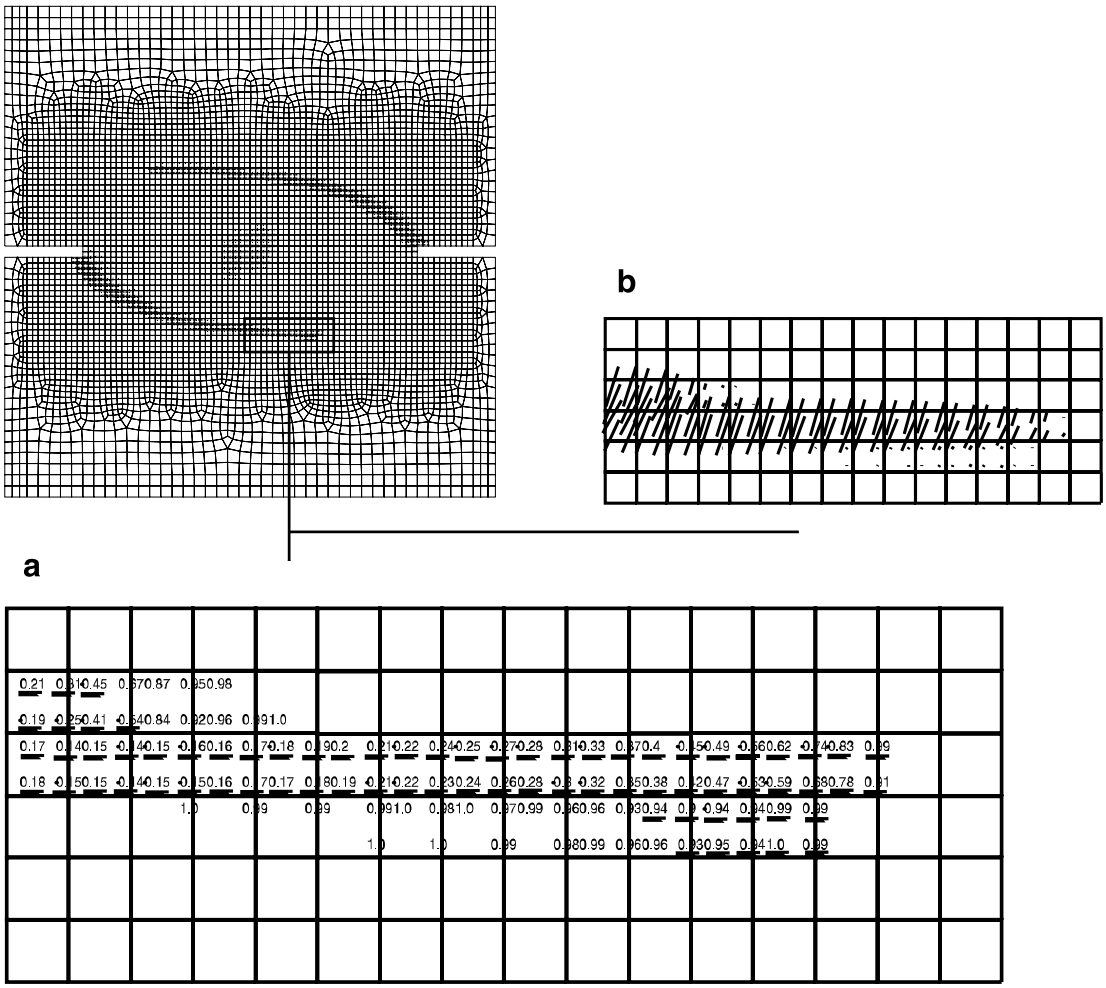

Fig. 12. Dissipative zone and damage values $\bar{\phi}_1$ in Fig. 8d.

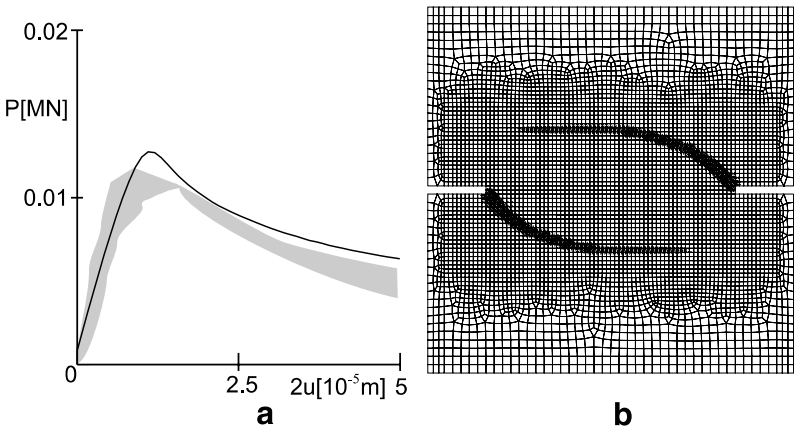

Fig. 13. Load–displacement curve (a) and damage path (b) at the displacement $2u = 5 \cdot 10^{-5}$ m, both for $h_{\mathrm{ch},1}$-approach.

Furthermore, regarding especially the sections close to the notches in Fig. 17, they seem to be even wider. This is founded by a bifurcation of the damage rate path at the begin of the second load step. Fig. 18 shows the damage rate path before the situation in Fig. 17(a) is attained. Two damage rate paths start growing at every notch in Fig. 18(a). The Fig. 18(b)–(d) reveal

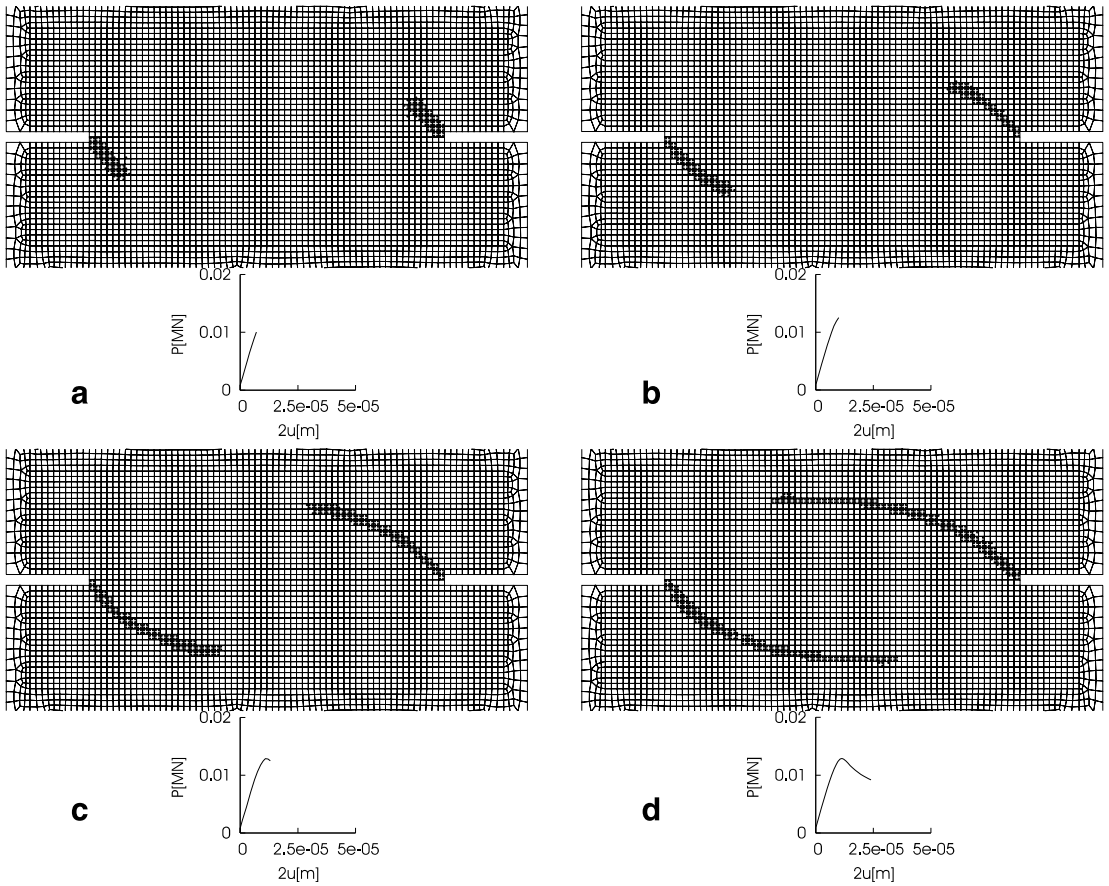

Fig. 14. Evolution of the damage rate path (dissipative zone) for $h_{ch,1}$-approach.

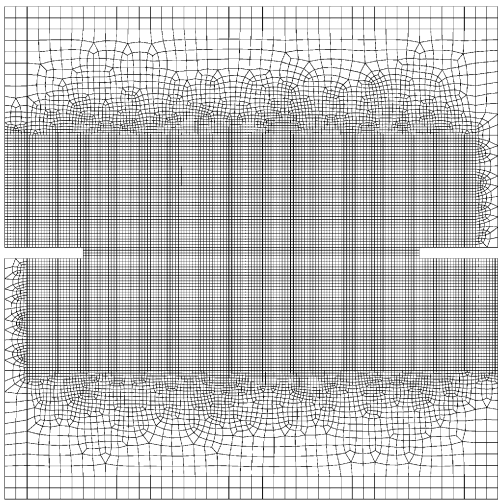

Fig. 15. Finer discretization.

that one becomes dominant and the second vanishes. The bifurcation has two consequences: the first consequence is that during the bifurcation in Fig. 18(a)–(d), the width of the dissipative zone is too wide what results in a too high energy consumption for increasing damage during these loading stages. This means that too much energy must be consumed in order to degrade the material. The second consequence is that the damage rate path is directly at the notches a bit too steep as long as

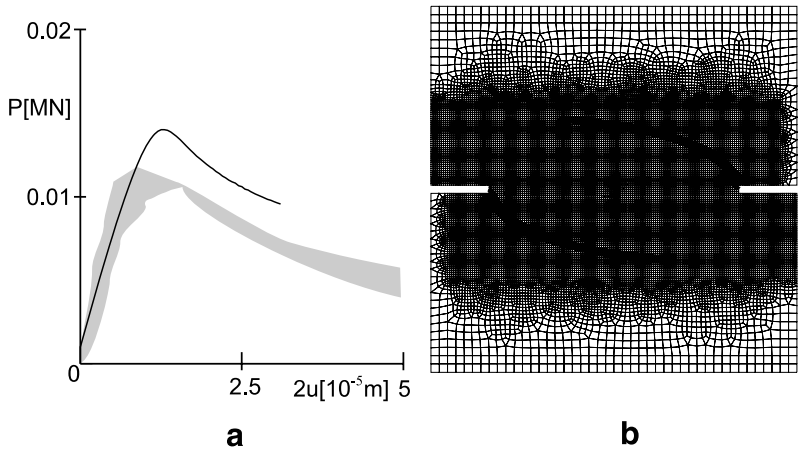

Fig. 16. Load–displacement curve (a) and damage path (b) of the finer mesh at the displacement $2u = 5 \cdot 10^{-5}$ m, both for $h_{\mathrm{ch},1}$-approach.

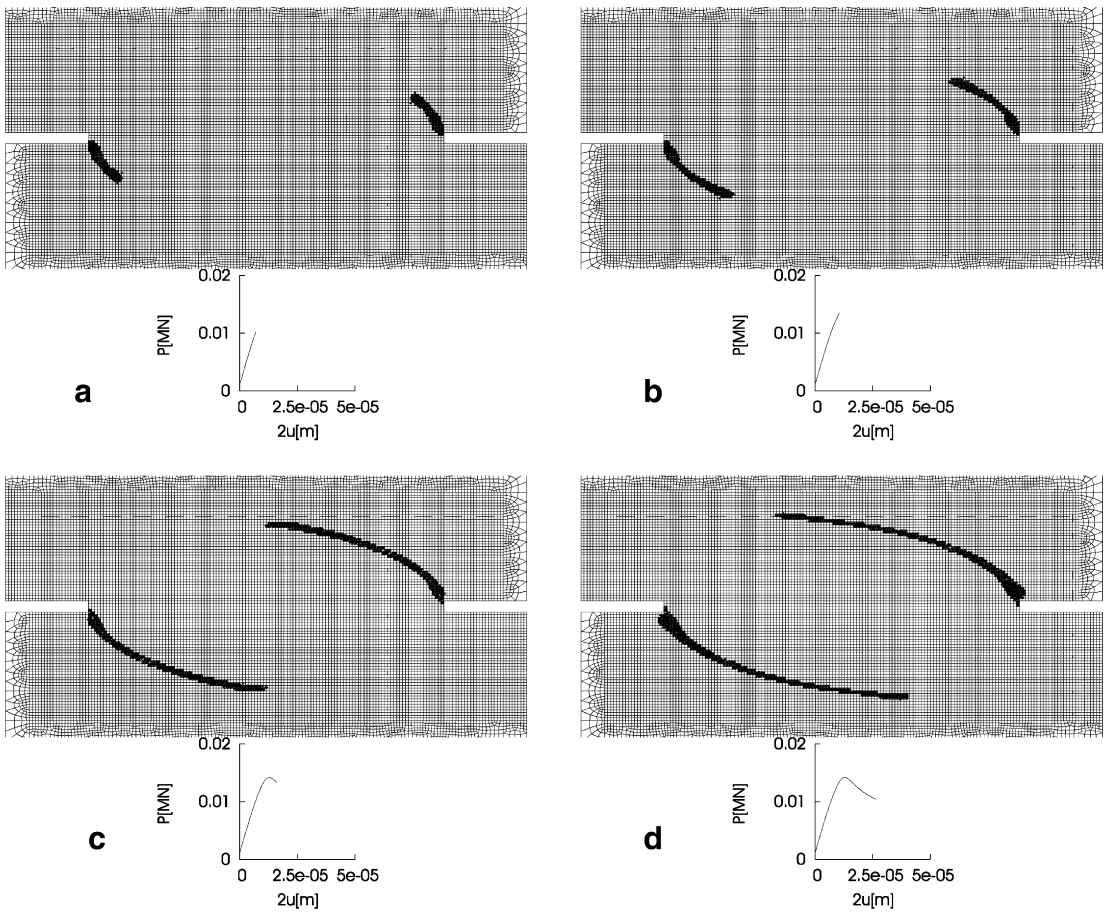

Fig. 17. Evolution of the damage rate path (dissipative zone) in the finer mesh for $h_{\mathrm{ch},1}$-approach.

the second path has not vanished, see Fig. 18(a)–(d). After the second path vanished, the damage rate path seems to continue growing less steep. In this too steep parts very close to the notches, the damage rate path remains too wide, see Fig. 17(a)–(d), what yields again a too high energy consumption for increasing damage.

Hence, two effects were observed in the damage rate path in the finer mesh deviating from the observations in the coarse mesh. Both effects yield a too wide h_{sim} in comparison to the assumed width $h_{\mathrm{ch},1}$ what results in a too high energy consump-

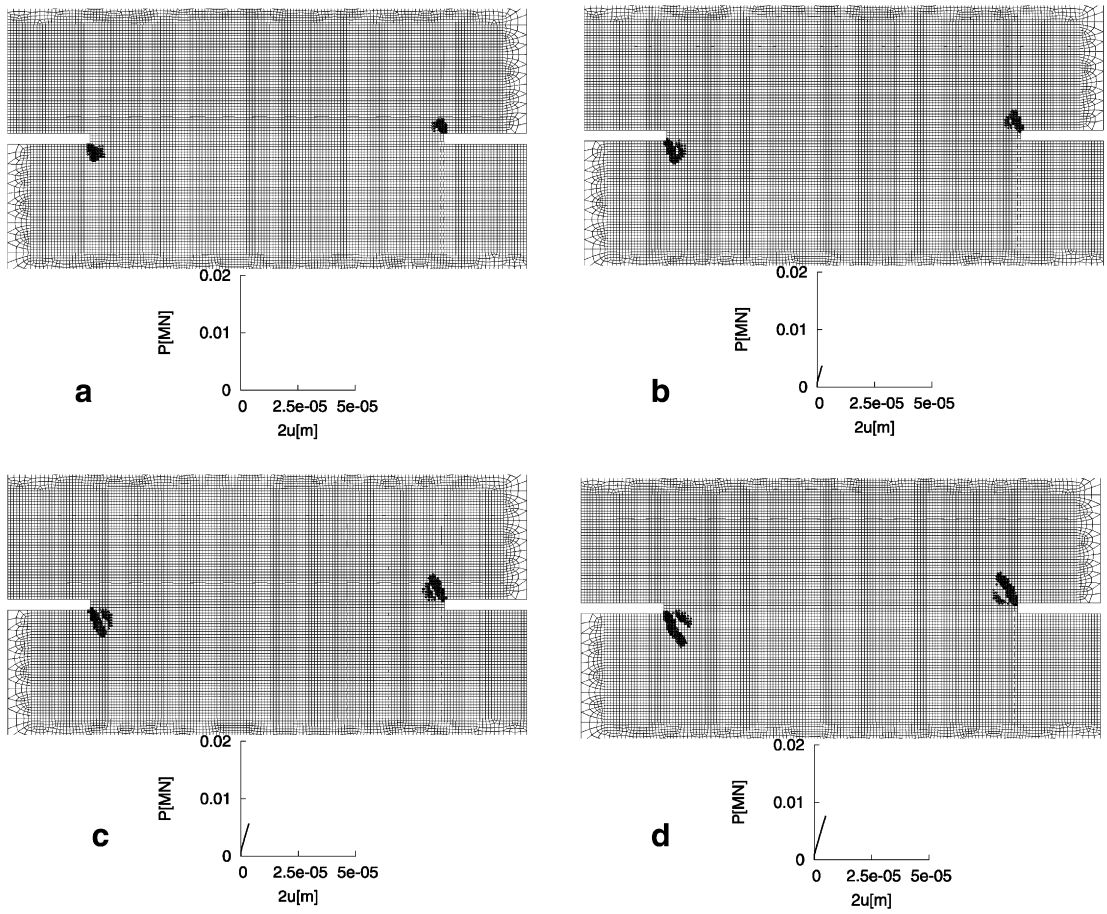

Fig. 18. Bifurcation of the damage rate path.

tion for increasing damage. Within the suggested theory of assuming a linear approach $h_{\mathrm{ch},1}$, the bifurcation problem cannot be solved. But the other effect, the damage rate path being generally $0.5l_e$—$1.0l_e$ wider in the fine mesh, can be taken into account by modifying the $h_{\mathrm{ch},1}$-approach.

In order to attain an adapted approach $h_{\mathrm{ch},1b}$ for the fine mesh, two boundary conditions of the $h_{\mathrm{ch},1}$-approach are substituted. First, the boundary condition for intact material in the curved path, $h_{\mathrm{ch},1}(\bar{\phi}_1 = 1, \alpha_1 = \pi/6) = 3.5 \cdot l_e$, is substituted by $h_{\mathrm{ch},1b}(\bar{\phi}_1 = 1, \alpha_1 = \pi/6) = 4.0 \cdot l_e$. Furthermore, similar considerations for the fine mesh as in Fig. 12(a) for the coarse mesh yielded the substitution of $h_{\mathrm{ch},1}(\bar{\phi}_1 = 0.4, \alpha_1 = \pi/18) = 1 \cdot l_e$ by $h_{\mathrm{ch},1b}(\bar{\phi}_1 = 0.6, \alpha_1 = \pi/18) = 1 \cdot l_e$. This yields the modified approach

$$h_{\mathrm{ch},1b}(\bar{\phi}_1, \alpha_1) = (-1.5 + 2.5 \cdot \bar{\phi}_1 + 5.73 \cdot \alpha_1) l_e, \tag{34}$$

with the restriction that, at any stage, $h_{\mathrm{ch},1} \geqslant l_e$ holds. The results of the simulation by applying the $h_{\mathrm{ch},1b}$-approach reveal the Figs. 19 and 20. The $h_{\mathrm{ch},1b}$-approach and the width h_{sim} show an acceptable coincidence in Fig. 20, better than the coincidence of the $h_{\mathrm{ch},1}$-approach with h_{sim} in Fig. 17. The peak load is still overestimated, but less in comparison to Fig. 16(a).

The load-displacement curves of the simulations applying the $h_{\mathrm{ch},1}$-approach in the coarse mesh and the $h_{\mathrm{ch},1b}$-approach in the fine mesh are both given in Fig. 21. It is very interesting to see that the difference between the two curves is quite small. Only the peak load is slightly higher in the simulation with the finer mesh. The reason is the above mentioned bifurcation effect.

But the coincidence of the two curves is absolutely sufficient for engineering applications. The same holds for the simulated peak load. The experimentally observed peak load is overestimated by approximately 10–15% what is an acceptable result for most engineering applications.

Additionally to the simulations using the $h_{\mathrm{ch},1}$- and $h_{\mathrm{ch},1b}$-approaches, five further simulations were performed where the refined mesh was kept fixed and a constant parameter h_{ch} was used in every simulation. The parameter was varied from 1 up to 5 times the element length. The characteristics of the evolution of the damage rate paths are similar to the observations in Figs. 3–10. Therewith, the discussion is less detailed. Fig. 22 shows the load–displacement curves of the five calculations with the fine mesh and the results of the coarse mesh, too. The load-displacement curves of the simulations b, d, e stop earlier

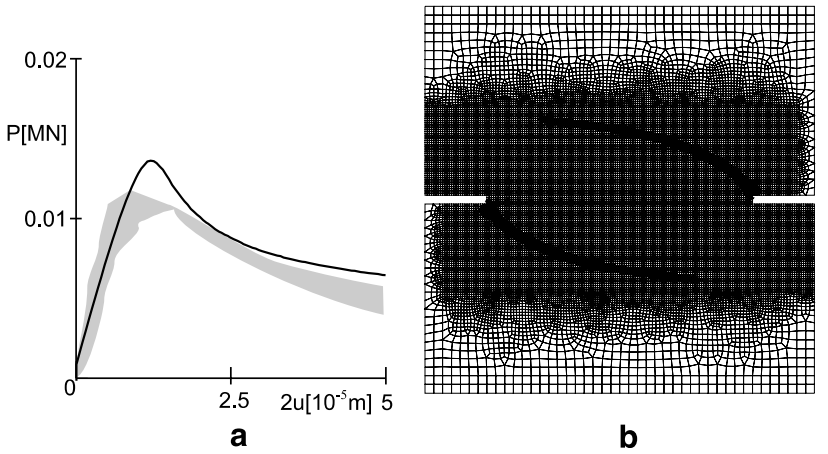

Fig. 19. Load–displacement curve(a) and damage path(b) of the finer mesh at the displacement $2u = 5 \cdot 10^{-5}$m, both for $h_{\mathrm{ch},1b}$-approach.

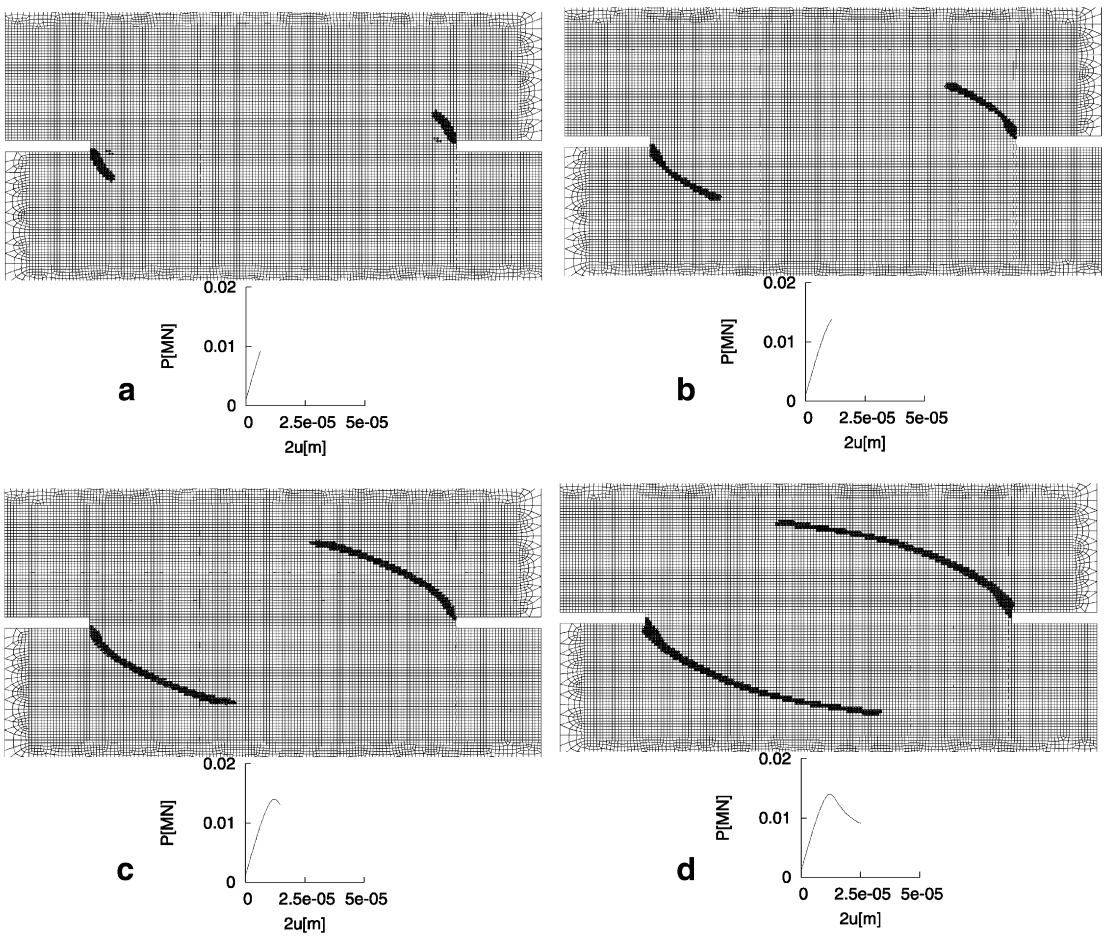

Fig. 20. Evolution of the damage rate path (dissipative zone) in the finer mesh for $h_{\mathrm{ch},1b}$-approach.

because the iterations lasted longer and the maximum computing time was reached. All calculations were executed at the High Performance Computing-Systems at ZIH in Dresden where the maximum computing time amounts three days. When considering Fig. 22, two essential features can be observed:

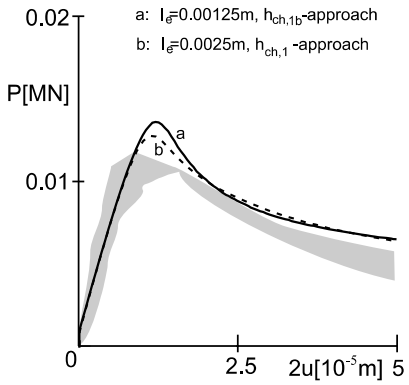

Fig. 21. Load–displacement curves for $h_{ch,1}$-approach in the coarse mesh and the $h_{ch,1b}$-approach in the fine mesh.

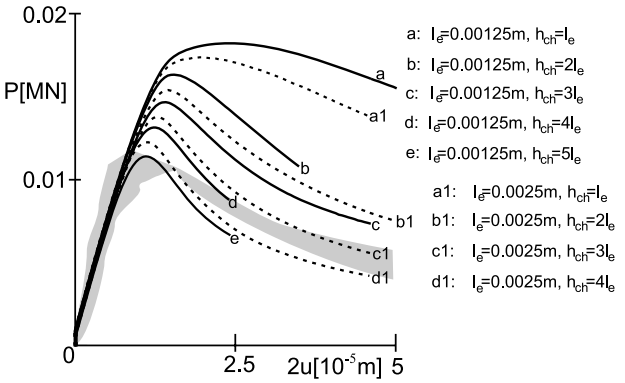

Fig. 22. Load–displacement curves for constant h_{ch} and both discretizations.

- The smaller the chosen width h_{ch} is, the higher is the simulated peak load and the ductility of the post peak behavior is increasing. The reason is that the energy consumption being necessary for progressive damage is increasing with decreasing width h_{ch}.
- The peak load in the simulations with the fine mesh is always slightly higher than the corresponding peak load resulting from the calculations using the coarse mesh. The main reason is that h_{sim} is always slightly wider in the simulations with the finer mesh. This validates the above mentioned observation that an approach for the width of the dissipative zone must depend on the discretization, too.The second, less important reason for the higher peak loads in the simulations with the finer mesh is the above explained bifurcation effect.

Finally, a last comment to the range of the h_{ch}-approaches in the literature, $h_{ch} \approx 1l_e..2l_e$, see e.g. (Rots, 1988; Oliver, 1989; Cervenka, 1995; Lackner, 1999; Winkler, 2001) or (Pölling, 2000). Considering the four curves when the width h_{ch} is chosen as $h_{ch} = 1l_e$ and $h_{ch} = 2l_e$ reveals a drastically overestimated peak load in all curves, see the curves $a1, b1, a, b$ in Fig. 22. If simulations with the applied meshes are performed by using the approaches for h_{ch} from the literature, the resulting load-displacement curves will all lie approximately between the a-curve and the $b1$-curve.

4. Conclusions

This paper presented an orthotropic model for the tensile behavior of concrete in a general three-dimensional formulation where the pseudo-log damage rate as suggested by Carol et al. (2001a) was used to simplify the definition of the loading surfaces. The model contains three decoupled loading functions in which every loading function takes into account one of the three principal directions of the orthotropic damage. The evolution rule for damage is derived by using the principle of maximum energy dissipation rate. In order to use the model for arbitrary simulations, the fracture energy approach is applied as a regularization technique. In this approach, the stress–crack opening relationship for the tensile behavior of concrete must be related to a characteristic length h_{ch} to obtain the stress–strain law.

The physical meaning of the characteristic length h_{ch} is the assumed width of the dissipative zone appearing in the simulation, this is one basic assumption in the paper. Because the width of the dissipative zone is not known in advance, the assumed width h_{ch} is a chosen parameter. In order to obtain the same energy dissipation as occurs in reality, the chosen

parameter h_{ch} should coincide with the width h_{sim} of the dissipative zone appearing in the simulation. The problem is that the chosen value for h_{ch} massively influences the width h_{sim} of the dissipative zone in the simulation.In order to study these phenomena, a series of simulations was performed with varying parameter h_{ch}. In every simulation, the evolution of the dissipative zone was investigated, especially the width h_{sim}. The following features were observed:

- The smaller the chosen width h_{ch} is, the wider the width h_{sim} of the dissipative zone in the simulations.
- The width h_{sim} decreases with increasing distance from the tip of the damage path. Because the damage increases with increasing distance from the tip, it follows that the width h_{sim} decreases with increasing damage at the specific material point.
- The width h_{sim} increases with increasing angle between the damage path and the element edges.

Based on these observations and analysis of plots that show the dissipative zone together with the damage at every integration point, an approach $h_{ch,1}(\bar{\phi}_1, \alpha_1)$ for the characteristic length was formulated which depends on the damage $\bar{\phi}_1$ and the inclination angle α_1 between the damage and the element edges.

A simulation by applying this approach sufficiently matched the experimentally observed peak load and showed good agreement of the assumed width of the dissipative zone $h_{ch,1}$ with the width h_{sim} of the dissipative zone appearing in the simulation.

In order to evaluate the theory and the suggested approach, six further simulations were performed applying a refined discretization. The same characteristics in the evolution of the dissipative zone were observed. However, the width h_{sim} is always 0.5—1.0 times the element length wider in comparison to the simulations using the coarse mesh.

Hence, a modified approach $h_{ch,1b}$ was suggested. A simulation with the finer mesh and the modified $h_{ch,1b}$-approach showed a good coincidence of the assumed width $h_{ch,1b}$ with the appearing width h_{sim} and yielded approximately the same load-displacement relationship as the simulation with the coarse mesh and the $h_{ch,1}$-approach. Therefore, it can be concluded that objective simulations are possible, if the requirement is fulfilled that the characteristic length in the constitutive law always approximately conforms to the width of the dissipative zone appearing in the simulation. Objectivity means here mesh independence. Of course, this objectivity is not exact, but absolutely sufficient for engineering applications.

The presented investigations showed that the current approach of using a characteristic length depending only on the inclination angle of the damage path to the element edges, (Rots, 1988; Oliver, 1989; Cervenka, 1995; Lackner, 1999; Pölling, 2000) or (Winkler, 2001), is not sufficient.

The suggested model has only four material parameters, the Young's modulus, the Poisson's ratio, the tensile strength and the fracture energy. The suggested regularization technique consists of two steps. First, an approach for the evolution of the width of the dissipative zone is formulated, and in the second step, the convenience of the approach is evaluated by comparing the approach with the evolution of the simulated dissipative zone. They must approximately correspond in order to reach a correct energy dissipation what yields mesh-independent results. In this paper, an approach based on simulations of a double edge notched specimen was suggested. Perhaps modifications are necessary when other experiments are considered. The approaches may slightly differ when various experiments are simulated with different element types or meshes but the requirement that the approach must approximately coincide with the width h_{sim} appearing in the simulation must be fulfilled. If this requirement is fulfilled, the simulations are objective. This is the basic message of the paper.

References

Aifantis, E.C., 1984. On the microstructural origin of certain inelastic models. Journal of Engineering Materials and Technology (106), 326–330.

Bažant, Z.P., 1976. Instability, ductility and size effect in strain-softening concrete. Journal of the Engineering Mechanics Division 102 (2), 331–344.

Bažant, Z.P., Cedolin, L., 1980. Blunt Crack Band Propagation in Finite Element Analysis. Journal of the Engineering Mechanics Division, 105 (EM2), Proc. Paper 14529, 297–315.

Bažant, Z.P., Oh, B.H., 1983. Crack band theory for fracture of concrete. Materials and Structures 16 (93), 155–177.

Berthaud, Y., Laborderie, C., Ramtani, S., 1990. Damage modelling and crack closure effekt. In: Ju, J., Krajcinovic, D., Schreyer, H., (Eds.), Damage Mechanics in Engineering Materials, New York, pp. 263–276.

Carol, I., Rizzi, E., Willam, K., 1994. A unified theory of elastic degradation and damage based on a loading surface. International Journal of Solids and Structures 31 (20), 2835–2855.

Carol, I., Rizzi, E., Willam, K., 2001a. On the formulation of anisotropic elastic degradation. I. Theory based on a pseudo logarithmic damage tensor rate. International Journal of Solids and Structures 4 (38), 491–518.

Carol, I., Rizzi, E., Willam, K., 2001b. On the formulation of anisotropic elastic degradation. II. Generalized pseudo-Rankine model for tensile damage. International Journal of Solids and Structures 4 (38), 519–546.

Cervenka, V., 1995. Mesh sensitivity effects in smeared finite element analysis of concrete fracture. In: Wittmann, F. (Ed.), Fracture Mechanics of Concrete and Concrete Structures (FraMCoS-2), pp. 1387-1396.

Chaboche, J., 1993. Development of continuum damage mechanics for elastic solids sustaining anisotropic and unilateral damage. International Journal of Damage Mechanics (2), 311–329.

Cosserat, E., Cosserat, F., 1909. Théorie des corps déformables. A. Herrman et Fils, Paris.

Dragon, A., Halm, D., Désoyer, T., 2000. Anisotropic damage in quasi-brittle solid: modelling, computational issues and applications. Computer Methods in Applied Mechanics and Engineering (183), 331–352.

Grassl, P., Jirasék, M., 2005. Plastic model with nonlocal damage applied to concrete. International Journal for Numerical and Analytical Methods in Geomechanics (30), 71–90.

Gopalaratnam, V., Shah, S.P., 1985. Softening response of plain concrete in direct tension. ACI Journal 82 (3), 311–323.

Govindjee, S., Kay, G.J., Simo, J.C., 1995. Anisotropic modelling and numerical simulation of brittle damage in concrete. International Journal for Numerical Methods in Engineering 38 (21), 3611–3633.

Hesebeck, O., 2000. Zur Modellierung von Schädigungsprozessen in elastoplastischen Materialien. Ph.D. thesis, Universität Karlsruhe.

Hill, R., 1958. A general theory of uniqueness and stability in elastic–plastic solids. Journal of the Mechanics and Physics of Solids (6), 236–249.
Krajcinovic, D., Fonseka, G., 1981. The continuous damage theory of brittle materials; part 1. General theory. Journal of Applied Mechanics (48), 809–815.
Krajcinovic, D., 1996. Damage mechanics, volume 41 of North-Holland Series In Applied Mathematics and Mechanics. Elsevier.
Lackner, R., 1999. Berechnungen von Flächentragwerken aus Stahlbeton mittels adaptiver Finiter Elemente. Ph.D. thesis, Technische Universität Wien.
Lemaitre, J., 1991. A Course on Damage Mechanics. Springer.
Luenberger, D.G., 1984. Linear and Nonlinear Programming. Addison-Wesley Publishing Company.
Murakami, S., Kamiya, K., 1996. Constitutive and damage evolution equations of elastic-brittle materials based on irreversible thermodynamics. International Journal of Mechanical Science 39 (4), 473–486.
Nooru-Mohamed, M., 1992. Mixed-mode fracture of concrete. Ph.D. thesis, Delft University of Technology.
Oliver, J., 1989. A consistent characteristic length for smeared cracking models. International Journal for Numerical Methods in Engineering (28), 461–474.
Oliver, J., 1996. Modelling strong discontinuities in solid mechanics via strain softening constitutive equations. Part 1: Fundamentals, Part 2: Numerical Simulation. International Journal for Numerical Methods in Engineering (39), 3575–3623.
Papa, E., Taliercio, A., 1996. Anisotropic damage model for the multiaxial static and fatigue behaviour of plain concrete. Engineering Fracture Mechanics 55 (2), 163–179.
Patzák, B., Jirasék, M., 2002. Process zone resolution by extended finite elements. Engineering Fracture Mechanics (70), 957–988.
Pölling, R., 2000. Eine praxisnahe, schädigungsorientierte Materialbeschreibung von Stahlbeton für Strukturanalysen. Ph.D. thesis, Ruhr-Universität Bochum.
Pröchtel, P., Häußler-Combe, U., 2007. Anisotropic damage of concrete: A three-dimensional approach with energy-based loading surfaces and a new evolution law. In: Carpinteri, A.; Gambarova, P.G.; Ferro, G.; Plizzari, G.A. (Eds.), Fracture Mechanics of Concrete and Concrete Structures (FraMCoS-6). Volume 1: New Trends in Fracture Mechanics of Concrete, 17.06.-22.06.2007, Catania (Italy), PP. 393-402.
Rizzi, E., Carol, I., Willam, K., 1996. Localization analysis of elastic degradation with application to scalar damage. Journal of Engineering Mechanics (121), 541–554.
Rots, J., 1988. Computational modeling of concrete fracture. Ph.D. thesis, TU Delft.
Saouridis, C., Mazars, J., 1992. Prediction of the failure and size effect in concrete via bi-scale damage approach. Engineering Computations (9), 329–344.
Simo, J., Ju, J., 1987a. Strain and stress-based continuum damage models-I. Formulation. International Journal of Solids and Structures 23 (7), 821–840.
Simo, J., Ju, J., 1987b. Strain and stress-based continuum damage models-II. Computational aspects. International Journal of Solids and Structures 23 (7), 841–869.
Simo, J., Oliver, J., Armero, F., 1993. An analysis of strong discontinuities induced by strain softening in rate-independent inelastic solids. Computational Mechanics (12), 277–296.
Winkler, B., 2001. Traglastuntersuchungen von unbewehrten und bewehrten Betonstrukturen. Ph.D. thesis, University of Innsbruck.